ALMA Survey of Orion Planck Galactic Cold Clumps (ALMASOP): Discovery of an extremely dense and compact object embedded in the prestellar core G208.68-19.92-N2

Naomi Hirano, Dipen Sahu, Sheng-Yaun Liu, Tie Liu, Ken'Ichi Tatematsu, Somnath Dutta, Shanghuo Li, Chin-Fei Lee, Pak Shing Li, Shih-Ying Hsu, et al.

The Astrophysical Journal, 961:123 (23pp), 2024 January 20 https://doi.org/10.3847/1538-4357/ad09e2

ALMA Survey of Orion Planck Galactic Cold Clumps (ALMASOP): Discovery of an Extremely Dense and Compact Object Embedded in the Prestellar Core G208.68-19.92-N2

Naomi Hirano[1], Dipen Sahu[1,2], Sheng-Yaun Liu[1], Tie Liu[3], Ken'ichi Tatematsu[4], Somnath Dutta[1], Shanghuo Li[5], Chin-Fei Lee[1], Pak Shing Li[3], Shih-Ying Hsu[1], Sheng-Jun Lin[1], Doug Johnstone[6,7], Leonardo Bronfman[8], Huei-Ru Vivien Chen[9], David J. Eden[10], Yi-Jehng Kuan[1,11], Woojin Kwon[12,13], Chang Won Lee[14,15], Hong-Li Liu[16], Mark G. Rawlings[17], Isabelle Ristorcelli[18], and Alessio Traficante[19]

[1] Academia Sinica Institute of Astronomy and Astrophysics, 11F of Astronomy-Mathematics Building, AS/NTU, No.1, Sec. 4, Roosevelt Road, Taipei 10617, Taiwan, R.O.C.; hirano@asiaa.sinica.edu.tw
[2] Physical Research laboratory, Navrangpura, Ahmedabad, Gujarat 380009, India
[3] Shanghai Astronomical Observatory, Chinese Academy of Sciences, 80 Nandan Road, Shanghai 200030, People's Republic of China
[4] Nobeyama Radio Observatory, National Astronomical Observatory of Japan, National Institutes of Natural Sciences, 462-2 Nobeyama, Minamimaki, Minamisaku, Nagano 384-1305, Japan
[5] Max Planck Institute for Astronomy, Königstuhl 17, D-69117 Heidelberg, Germany
[6] NRC Herzberg Astronomy and Astrophysics, 5071 West Saanich Road, Victoria, BC, V9E 2E7, Canada
[7] Department of Physics and Astronomy, University of Victoria, Victoria, BC, V8P 5C2, Canada
[8] Departamento de Astronomía, Universidad de Chile, Camino el Observatorio 1515, Las Condes, Santiago, Chile
[9] Institute of Astronomy and Department of Physics, National Tsing Hua University, Hsinchu, 30013, Taiwan, R.O.C.
[10] Armagh Observatory and Planetarium, College Hill, Armagh, BT61 9DB, UK
[11] Department of Earth Sciences, National Taiwan Normal University, Taipei, Taiwan, R.O.C.
[12] Department of Earth Science Education, Seoul National University, 1 Gwanak-ro, Gwanak-gu, Seoul 08826, Republic of Korea
[13] SNU Astronomy Research Center, Seoul National University, 1 Gwanak-ro, Gwanak-gu, Seoul 08826, Republic of Korea
[14] Korea Astronomy and Space Science Institute, 776 Daedeokdae-ro, Yuseong-gu, Daejeon 34055, Republic of Korea
[15] University of Science and Technology, Korea (UST), 217 Gajeong-ro, Yuseong-gu, Daejeon 34113, Republic of Korea
[16] Department of Astronomy, Yunnan University, and Key Laboratory of Particle Astrophysics of Yunnan Province, Kunming, 650091, People's Republic of China
[17] Gemini Observatory/NSF's NOIRLab, 670 N. A'ohoku Place, Hilo, Hawai'i, 96720, USA
[18] IRAP, Université de Toulouse, CNRS, 9 avenue du Colonel Roche, BP 44346, 31028 Toulouse Cedex 4, France
[19] IAPS-INAF, via Fosso del Cavaliere 100, I-00133, Rome, Italy
Received 2023 July 7; revised 2023 October 26; accepted 2023 November 4; published 2024 January 18

Abstract

The internal structure of the prestellar core G208.68-19.02-N2 (G208-N2) in the Orion Molecular Cloud 3 (OMC-3) region has been studied with the Atacama Large Millimeter/submillimeter Array. The dust continuum emission revealed a filamentary structure with a length of ∼5000 au and an average H_2 volume density of $\sim 6 \times 10^7$ cm^{-3}. At the tip of this filamentary structure, there is a compact object, which we call a *nucleus*, with a radius of ∼150–200 au and a mass of ∼0.1 $M_\odot$. The nucleus has a central density of $\sim 2 \times 10^9$ cm^{-3} with a radial density profile of $r^{-1.87\pm0.11}$. The density scaling of the nucleus is ∼3.7 times higher than that of the singular isothermal sphere (SIS). This as well as the very low virial parameter of 0.39 suggests that the gravity is dominant over the pressure everywhere in the nucleus. However, there is no sign of CO outflow localized to this nucleus. The filamentary structure is traced by the N_2D^+ 3–2 emission, but not by the $C^{18}O$ 2–1 emission, implying the significant CO depletion due to high density and cold temperature. Toward the nucleus, the N_2D^+ also shows the signature of depletion. This could imply either the depletion of the parent molecule, N_2, or the presence of the embedded very-low luminosity central source that could sublimate the CO in the very small area. The nucleus in G208-N2 is considered to be a prestellar core on the verge of first hydrostatic core (FHSC) formation or a candidate for the FHSC.

Unified Astronomy Thesaurus concepts: Molecular clouds (1072); Collapsing clouds (267); Star forming regions (1565); Star formation (1569); Astrochemistry (75); Early stellar evolution (434)

1. Introduction

Dense, cold, and gravitationally unstable starless cores prior to the onset of star formation, so-called "prestellar cores," are ideal targets for studying the initial condition of protostellar collapse (e.g., di Francesco et al. 2007; Ward-Thompson et al. 2007). Studying the physical conditions such as temperature, density, and gas kinematics of prestellar cores is essential to understand how the cores collapse and initiate star formation.

The Planck Galactic Cold Clumps (PGCCs; Planck Collaboration et al. 2016) are considered as the ideal targets for studying the initial condition of star formation due to their low dust temperatures of 6–20 K. Using the 15 m James Clerk Maxwell Telescope (JCMT) equipped with the Submillimeter Common User Bolometer Array-2 (SCUBA-2), the legacy survey "SCOPE: SCUBA-2 Continuum Observations of Pre-protostellar Evolution" has observed 1235 PGCCs at an angular resolution of 14.″4, and cataloged ∼3500 dense cores (Liu et al. 2018; Eden et al. 2019). In the Orion molecular

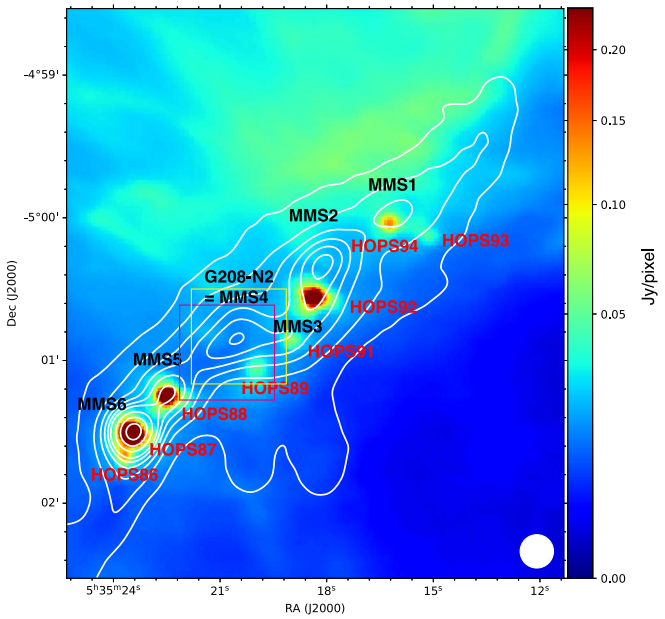

Figure 1. 850 μm continuum emission of the northern part of OMC-3 region including G208.68-19.20-north observed with the JCMT SCUBA-2 (Yi et al. 2018) in contours overlaid on the Hershel PACS 70 μm image in color. Contours are drawn every 5σ step with the lowest contour level of 5σ. 1σ level is 64.2 mJy beam^{-1}. White circle in the bottom right denotes the JCMT beam (14.″0). The names of the cores follow the nomenclature of Chini et al. (1997), and the protostellar sources in the HOPS catalog are given in the black and red letters, respectively. Magenta and yellow boxes denote the regions of Figures 2(a) and (c), respectively.

cloud complex including Orion A, Orion B, and λ Orionis regions, the SCOPE survey identified 119 dense cores (Yi et al. 2018). These cores are further studied in molecular lines at the 3 mm band using the Nobeyama Radio Observatory (NRO) 45 m telescope (Tatematsu et al. 2017; Kim et al. 2020; Tatematsu et al. 2021, 2022). Using the N_2D^+ 1–0 intensity observed with the NRO 45 m telescope, 72 Orion dense cores have been selected; 23 out of 72 have no mid-infrared source in the Wide-Field Infrared Survey Explorer (WISE) catalog (Wright et al. 2010), while 49 have WISE sources. The selected starless cores show intense N_2D^+ emission, and are considered to be in the evolved starless stage close to the onset of star formation. The sample of protostellar cores include the ones with and without intense N_2D^+ emission. The former with intense N_2D^+ are considered to be in an earlier evolutionary stage than the latter without N_2D^+ emission. Therefore, the selected 72 dense cores cover the evolutionary stages before and after the onset of star formation. The "Atacama Large Millimeter/submillimeter Array (ALMA) Survey of Orion PGCCs (ALMASOP)" project has observed these 72 dense cores at high angular resolution in the continuum and molecular lines at 1.3 mm in order to study the fragmentation and substructures of dense cores at the onset of star formation. The description and the full sample of ALMASOP are presented in Dutta et al. (2020).

G208.68-19.20-N2 (G208-N2) is one of the SCUBA-2 cores identified in the PGCC G208.68-19.20 North (Yi et al. 2018), which corresponds to the northern part of the Orion Molecular Cloud 3 (OMC-3). The SCUBA-2 850 μm continuum image of the OMC-3 region including G208.68-19.20 North on top of the Herschel PACS 70 μm image from archive is shown in Figure 1. The distance to OMC-3 is estimated to be $\sim$390 pc (Kounkel et al. 2017, 2018; Tobin et al. 2020). This core was also identified in the previous observations at 1.3 mm (MMS4; Chini et al. 1997), 350 μm (CSO9; Lis et al. 1998), and 850 μm (OriAN-535207-50053; Nutter & Ward-Thompson 2007; SMM5; Takahashi et al. 2013). The 850 μm image at 4.″5 resolution obtained with the Submillimeter Array shows that this core is elongated along the northwest–southeast direction and surrounded by an envelope with a triangle shape (Takahashi et al. 2013). Figure 1 shows that there is an infrared source HOPS 89, which is classified as a flat spectrum source (Megeath et al. 2012; Furlan et al. 2016), to the southwest of the JCMT continuum peak of G208-N2 (Yi et al. 2018). However, this source is offset by $\sim$12″ from the JCMT continuum peak, and is located outside of the triangle-shaped envelope observed at 850 μm (Takahashi et al. 2013) and 1.3 mm (Dutta et al. 2020). Therefore, G208-N2 is likely to be starless.

The 3 mm line observations with the NRO 45 m telescope have revealed that the N_2H^+ 1–0 and N_2D^+ 1–0 intensity values of this core are the brightest among the 119 cores in the Orion region (Kim et al. 2020). The N_2D^+/N_2H^+ column density ratio in G208-N2 was estimated to be 0.11 $\pm$ 0.01 (Kim et al. 2020), indicating that this core is in the late evolutionary stage of the starless phase where $N(N_2D^+)/N(N_2H^+) > 0.1$ (Crapsi et al. 2007), likely to be close to the onset of star formation. This scenario is also supported by the 1.3 mm continuum observations of ALMASOP. Sahu et al. (2021) has reported the detection of a compact and dense substructure in five starless cores including G208-N2 at 1.″2 resolution. The sizes of the substructures in these cores, $\sim$2000 au, are comparable to that of the well-studied prestellar core, L1544 (Caselli et al. 2019). However, their average density, $\sim 10^7$ cm^{-3}, is ten times higher than that of L1544. They found that these five cores are gravitationally unstable prestellar cores. The 1.3 mm continuum emission from G208-N2 is the brightest among these five cores with substructures.

In this work, we utilize ALMASOP and archival ALMA data, and study the internal structure of G208-N2 using the continuum emission at 1.3 and 1.1 mm, and the molecular lines at 1.3 mm. Thanks to the high resolution and high sensitivity of ALMA, the continuum images have revealed an embedded compact object having a radius of $\sim$200 au and a central density of $\gtrsim 10^9$ cm^{-3}. We discuss the physical properties and the evolutionary stage of this compact object. We also study the chemical stratification in G208-N2 using the molecular line data of $C^{18}O$, N_2D^+, DCO^+, and H_2CO.

2. Observations

2.1. ALMASOP

The ALMA band 6 (1.3 mm) observations of G208-N2 were carried out as a part of the ALMASOP project in Cycle-6 (#2018.1.00302.S; PI; Tie Liu). The observations were executed in three different array configurations; 12 m array C43-5 (TM1), 12 m array C43-2 (TM2), and 7 m array of the Atacama Compact Array (ACA). The TM1, TM2, and ACA observations were conducted in three, one, and five execution blocks (EBs), respectively. The projected baseline lengths of these three configurations are from 9 to 1090 kλ in TM1, 9 to 240 kλ in TM2, and 5 to 36 kλ in ACA. Four spectral windows (SPWs) centered at the rest frequencies of 231.0, 233.0, 218.918, and 216.6178 GHz were used simultaneously. Each

Table 1
Summary of the Image Parameters

Project Code	Line or Continuum	Rest Frequency (GHz)	Synthesized Beam (arcsec, deg.)	UV Taper (arcsec.)	Spectral Resolution (km s^{-1})	rms Noise Level (mJy beam^{-1})
2018.1.00302.S	1.3 mm continuum	218/232	$0\farcs38 \times 0\farcs30$, −65.0	⋯	⋯	0.06
	1.3 mm continuum	218/232	$1\farcs16 \times 1\farcs04$, −63.4	$0\farcs9$	⋯	0.15
	CO 2–1	230.538000	$0\farcs41 \times 0\farcs31$, −64.1	⋯	1.47	2.8
	CO 2–1	230.538000	$1\farcs10 \times 0\farcs99$, −60.9	$0\farcs8$	1.47	4.0
	N_2D^+ 3–2	231.32187	$1\farcs11 \times 0\farcs99$, −60.7	$0\farcs8$	1.46	5.0
	$C^{18}O$ 2–1	219.5603541	$1\farcs11 \times 1\farcs00$, −59.9	$0\farcs8$	1.54	6.3
	H_2CO $3_{2,1}$–$2_{2,0}$	218.760066	$1\farcs13 \times 1\farcs02$, −61.8	$0\farcs8$	1.55	4.2
	H_2CO $3_{2,2}$–$2_{2,1}$	218.4756320	$1\farcs12 \times 1\farcs01$, −62.1	$0\farcs8$	1.55	4.2
	H_2CO $3_{0,3}$–$2_{0,2}$	218.2221920	$1\farcs10 \times 1\farcs03$, −73.9	$0\farcs8$	1.55	4.1
	DCN 3–2	217.2386307	$1\farcs11 \times 1\farcs00$, −59.4	$0\farcs8$	1.56	4.0
	SiO 5–4	217.1049800	$1\farcs12 \times 1\farcs00$, −60.1	$0\farcs8$	1.56	4.2
	DCO^+ 3–2	216.112580	$1\farcs12 \times 1\farcs01$, −59.4	$0\farcs8$	1.57	4.2
2015.1.00341.S	1.1 mm continuum	257/273	$0\farcs17 \times 0\farcs14$, +18.3	⋯	⋯	0.04
	1.3 mm continuum	217/230.5	$1\farcs52 \times 0\farcs88$, −77.2	⋯	⋯	0.40
	N_2D^+ 3–2	231.32187	$1\farcs53 \times 0\farcs91$, −77.9	⋯	0.10[a]	33
	$C^{18}O$ 2–1	219.5603541	$1\farcs58 \times 0\farcs93$, −77.3	⋯	0.10[a]	30
	CO 2–1	230.538000	$1\farcs50 \times 0\farcs89$, −77.9	⋯	0.32	10

Note.
[a] Spectral resolution of the image data cube.

SPW was set to a total bandwidth of 1.875 GHz and a spectral resolution of 1.129 MHz. The corresponding velocity resolution was ∼1.5 km s^{-1}. This spectral setting accommodates the $J = 2$–1 of CO and $C^{18}O$, $J = 3$–2 of N_2D^+, DCO^+, and DCN, three transitions of H_2CO, $3_{0,3}$–$2_{0,2}$, $3_{2,2}$–$2_{2,1}$, and $3_{2,1}$–$2_{2,0}$, and the SiO $J = 5$–4 lines. The total bandwidth for the continuum was 7.5 GHz. The details of the observational parameters are summarized in Dutta et al. (2020). The coordinates of the phase center for G208-N2 were $\alpha_{\rm ICRS} = 5^{\rm h}35^{\rm m}20\fs469$, $\delta_{\rm ICRS} = -5°00'50\farcs394$.

The visibility data of each EB were calibrated separately using the standard pipeline of CASA 5.4 (McMullin et al. 2007). The continuum visibility data were obtained by averaging the line-free channels of the four SPWs. The continuum emission was subtracted from the line data in the visibility domain. The calibrated visibility data of TM1, TM2, and ACA were combined, and imaged using the TCLEAN task of CASA 5.5. The maximum recoverable scale (MRS) was $38\farcs6$. In order to improve the signal-to-noise ratio, the molecular lines other than CO were imaged using the UV taper of $0\farcs8$ and the Briggs weighting with a robustness of +0.5, which provided the synthesized beam size of $1\farcs1 \times 1\farcs0$. The 1.3 mm continuum and CO 2–1 line were imaged with and without UV taper using the Briggs weighting with a robustness of +0.5. The beam size without UV taper is $0\farcs38 \times 0\farcs30$ with a position angle of −65.°0 for the 1.3 mm continuum, and is $0\farcs41 \times 0\farcs31$ with a position angle of −64.°1 for the CO 2–1. The UV taper for the 1.3 mm continuum was adopted to be $0\farcs9$, and that for CO 2–1 was adopted to be $0\farcs8$. The beam size and the rms noise level per channel of each molecular line are listed in Table 1.

2.2. 1.1 and 1.3 mm Data from the ALMA Archive

We also retrieved the archival ALMA band 6 data of G208-N2 observed in Cycle-3 (#2015.1.00341.S; PI; S. Takahashi). The 1.1 mm continuum data have been observed in the full polarization mode with the 12 m array. Two EBs were observed on 2016 September 16 with 38 antennas. The array configuration was C40-6, which provided the projected baseline range from 12 to 2280 kλ and the MRS of $3\farcs0$. Four SPWs with 1.875 GHz bandwidth centered at 256, 258, 272, and 274 GHz provided a total continuum bandwidth of 7.5 GHz. The phase center of this data set was set to be $\alpha_{\rm ICRS} = 5^{\rm h}35^{\rm m}20\fs88$, $\delta_{\rm ICRS} = -5°00'56\farcs25$. The bandpass calibrator, J0510+1800, and the flux calibrator, J0423-0120, were observed in the first EB. The phase and polarization calibrators for both EBs are J0541-0211 and J0522-3627, respectively. The bandpass and flux calibrations of the second EB without bandpass and flux calibrators have been done using the polarization calibrator, J0522-3627. The visibility data of each EB were calibrated manually using CASA 4.7.0. The Stokes *I*, *Q*, and *U* images were made using the TCLEAN task of CASA 6.4.0. The Briggs weighting with a robustness of +0.5 was adopted. The resulting beam size is $0\farcs17 \times 0\farcs14$ with a position angle of 18.°3. In this paper, we only use the Stokes *I* image. The rms noise level of the Stokes *I* image is 0.04 mJy beam^{-1}.

The 1.3 mm line and continuum observations have been done in the dual polarization mode. The coordinates of the phase center were the same as those of the 1.1 mm continuum data. Two SPWs including the N_2D^+ 3–2 and $C^{18}O$ 2–1 lines were set to the high spectral resolution mode with a 35.28 kHz resolution. The corresponding velocity resolutions were 0.046 km s^{-1} for the N_2D^+ and 0.048 km s^{-1} for the $C^{18}O$. The other two SPWs with 468.75 MHz bandwidth centered at 230.5 and 217.1 GHz were used for the continuum. The CO 2–1 line in the SPW centered at 230.5 GHz was also examined in order to search for the outflow emission. The spectral resolution of the CO 2–1 line is 244.171 kHz, which corresponds to the velocity resolution of 0.32 km s^{-1}. The images were made using the data obtained with the C36-1 configuration of the 12 m array and the ACA 7 m array. The observations with the C36-1 configuration were conducted on 2016 January 29. The projected baseline range was from 9 to 238 kλ. The bandpass calibrator was J0522-3627, which was also used for the flux calibration, and the phase calibrator was

J0541-541. The visibility data has been manually calibrated using CASA 4.7.2. The 7 m array observations were done in 4 EBs on 2016 June 30, July 12, 17, and 19. The projected baseline range was from 6 to 36 kλ. The bandpass, flux, and phase calibrators for the EB of July 12 were J0538-4405, J0854+2006, and J0607-0834, respectively. Those for the other three EBs were J0522-3627, J0522-3627, and J0542-0913, respectively. The visibility data were calibrated by the ALMA observatory using CASA 4.6.0.

The calibrated visibility data of the 12 m array and ACA were imaged together using the TCLEAN task of CASA 5.5 after continuum subtraction. The MRS of the combined data is 38.″8. The Briggs weighting with a robustness of +0.5 provided the resulting beam size of $\sim 1.''5 \times 0.''9$ for the N_2D^+, $C^{18}O$, CO, and 1.3 mm continuum. The rms noise level of the 1.3 mm continuum image is ~0.4 mJy beam $^{-1}$. The N_2D^+ and $C^{18}O$ lines were imaged every 0.1 km s^{-1}. The rms noise level per channel is ~33 mJy beam^{-1} for the N_2D^+, and is ~30 mJy beam^{-1} for the $C^{18}O$. The CO line was imaged with the original spectral resolution of 0.32 km s^{-1}. The rms noise level per channel is ~10 mJy beam^{-1}.

3. Results

3.1. 1.3 and 1.1 mm Continuum—A Compact Nucleus in the Filamentary Cloud

Figure 2 shows the 1.3 and 1.1 mm dust continuum images. Figures 2(a) and (b) are obtained with the combined TM1+TM2+ACA data of the ALMASOP project, and Figures 2(c) and (d) are the Stokes *I* images of the 1.1 mm archival polarization data. Figures 2(a) and (c) show that the continuum emission from G208-N2 exhibits the narrow filamentary structure with a position angle of ~120°, which is roughly the same as that of the OMC-3 ridge. The ALMASOP 1.3 mm image shows that the filament is surrounded by the triangle-shaped envelope, the outer boundary of which is indicated by the dashed triangle in Figure 2(a), the western extension of which is connected to the adjacent protostellar core, OMC-MMS3. This extended emission is not sampled in the 1.1 mm data due to the lack of the short spacing data. The bright point source in the southwestern part of the field of views in both Figures 2(a) and (c) is a flat spectrum young stellar object (YSO) HOPS 89 (Megeath et al. 2012; Furlan et al. 2016). It is obvious that HOPS 89 is not embedded in the dense filament traced by the 1.3 and 1.1 mm continuum emission.

To the eastern end of the filamentary structure, there is a compact source (hereafter referred as a *nucleus*). The position, peak flux density, integrated flux, and size of the nucleus were derived from the 2D Gaussian fitting in the image plane. The fitting results are summarized in Table 2. The peak flux densities at 1.3 and 1.1 mm correspond to the brightness temperatures of 0.27 and 0.64 K, respectively, which are much lower than the dust temperature at the center of prestellar cores, 6.5 K (Crapsi et al. 2007; Keto & Caselli 2010). This means that the beam-averaged continuum emission from the nucleus is optically thin at 1.3 and 1.1 mm. The size of the nucleus after deconvolved with the beam is 1.″34 (520 au) × 0.″82 (320 au) in the 1.3 mm image and is 0.″91 (360 au) × 0.″60 (230 au) in the 1.1 mm image. The nucleus is elongated along the east–west direction with a position angle of −82° in both 1.3 and 1.1 mm images. This direction is neither parallel nor perpendicular to the filamentary structure. The mass of the nucleus is calculated using the following formula:

$$M_{\rm gas} = \frac{F_\nu D^2}{\kappa_\nu B_\nu(T_{\rm dust})}, \quad (1)$$

where ν is the frequency corresponds to the observed wavelength, F_ν is the total integrated flux, D is the source distance, κ_ν is the dust mass opacity, $T_{\rm dust}$ is the dust temperature, and $B_\nu(T_{\rm dust})$ is the Planck function at a temperature of $T_{\rm dust}$. We adopt the theoretical dust opacity values of $\kappa_{230\ \rm GHz} = 0.011\ \rm cm^2 g^{-1}$, and $\kappa_{260\ \rm GHz} = 0.0145\ \rm cm^2 g^{-1}$ for the MRN size distribution (Mathis et al. 1977) with thin ice mantles at a number density of $10^8\ \rm cm^{-3}$ (Ossenkopf & Henning 1994), and a gas-to-dust ratio of 100. The dust temperature is assumed to be 11 K, which is the same as the N_2D^+ excitation temperature toward the nucleus derived from the hyperfine (hf) fitting (see Section 3.4.1). The derived mass is ~0.09 $M_\odot$. Assuming that the nucleus is a sphere with an effective radius of 150–200 au, the mean gas density is estimated to be (3.1–8.5)×10^8 cm^{-3}.

3.2. Dense Gas Tracers

Integrated intensity images of the molecular lines observed with the ALMASOP project are shown in Figure 3. The tapered image of the 1.3 mm continuum emission observed with the ALMASOP is overlaid on each panel. The tapered continuum image at ~1″ spatial resolution reveals that the triangle-shaped envelope surrounding the filament extends to the north and west. There is a secondary peak to the north of the triangle-shaped envelope (referred to as a *northern peak*). The continuum enhancement at the western edge of the field of view is the neighboring protostellar core MMS3 (Morii et al. 2021). The area enclosed by the 20% level contour has a size of 17.″5 (6,800 au)×3.″5 (1400 au) with an aspect ratio of ~5, and that within the 50% contour level has a size 12″ (4,700 au)×1.″5 (590 au) with an aspect ratio of ~8. The area within the 50% contour level is referred to as a *continuum filament*.

The $C^{18}O$ emission is distributed in the northeast and southwest of the field of view. The $C^{18}O$ emission extending to the west belongs to the neighboring core, MMS3. It is remarkable that the $C^{18}O$ emission is completely missing in the region traced by the continuum including the continuum filament, the triangle-shaped envelope, and the northern peak. In addition, there is no $C^{18}O$ emission in the vicinity of the nucleus. In contrast to the $C^{18}O$, the N_2D^+ shows a similar distribution as the continuum emission, as reported by Sahu et al. (2021). The N_2D^+ emission also comes from the northern peak and MMS3. The anticorrelation between the $C^{18}O$ and N_2D^+ is consistent with the picture that G208-N2 is an evolved starless core with CO depletion through freeze-out and high deuterium fractionation. It is also in contrast with the neighboring protostellar core, MMS5, in which the centrally condensed structure surrounding the protostar is traced well with $C^{18}O$ and barely seen in N_2D^+ (Matsushita et al. 2019). Although the spatial distribution of N_2D^+ correlates well with that of the dust continuum, the N_2D^+ emission is brighter in the western part, and is not enhanced at the nucleus.

The DCO^+ emission shows an elongated feature running parallel to the continuum filament. The DCO^+ ridge is systematically offset by ~2″ southward from the continuum filament, and delineates the southern edge of the triangle-shaped evelope. The DCO^+ emission peaks to the south of the

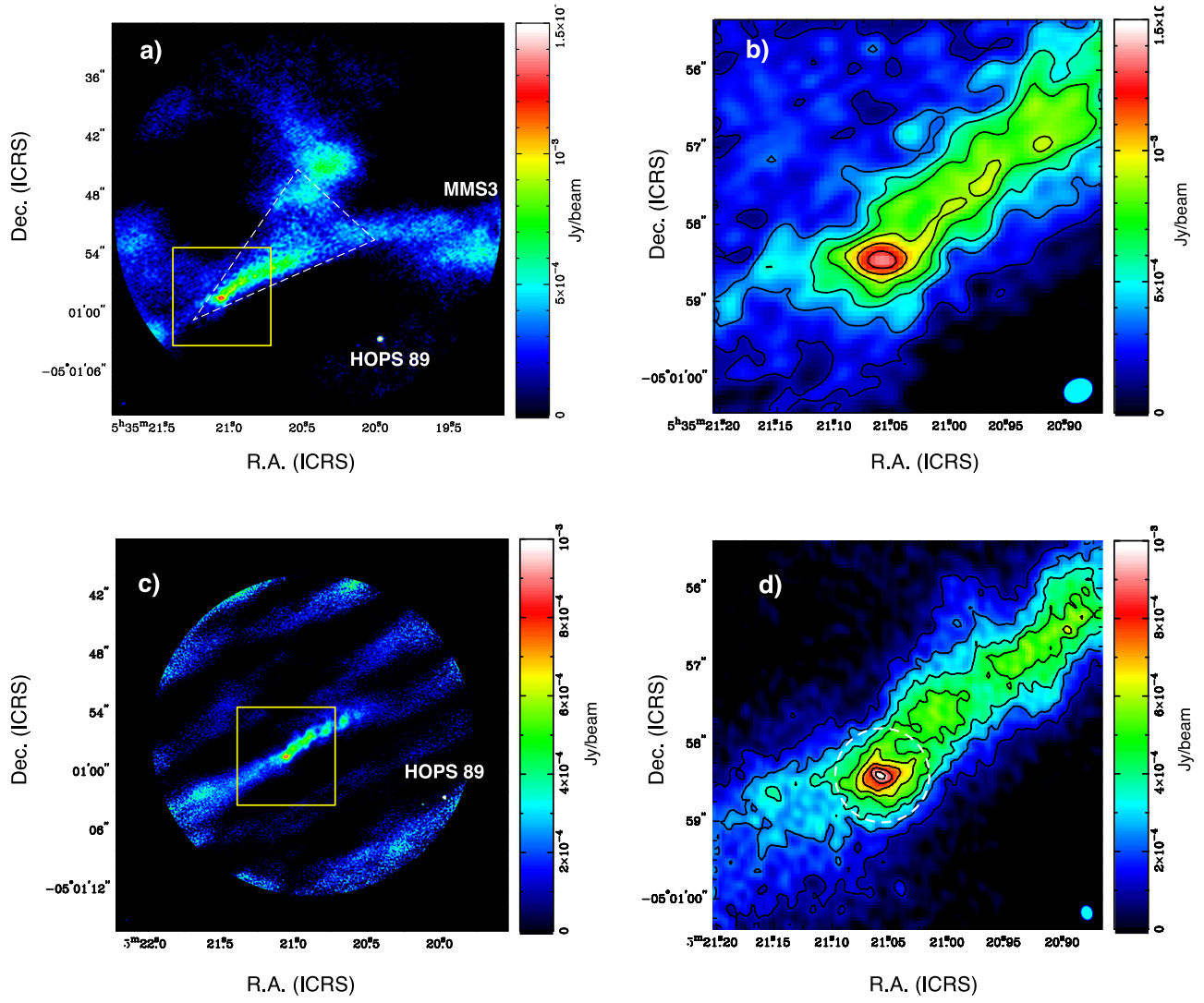

Figure 2. (a) ALMASOP 1.3 mm continuum emission image obtained using the combined TM1+TM2+ACA data without UV taper. Dashed triangle delineates the envelope surrounding the filamentary structure. The point source in the southwestern part of the field of view is a flat spectrum YSO HOPS 89 (Megeath et al. 2012; Furlan et al. 2016). (b) A close-up view of the yellow box in panel (a) including the *nucleus*. Contours are drawn every 3σ with the lowest contour of 3σ. The 1σ level is 0.06 mJy beam^{-1}. The synthesized beam ($0\farcs38 \times 0\farcs30$ with a P.A. of $-65\fdg0$) is drawn as a cyan ellipse in the bottom right corner. (c) 1.1 mm continuum image obtained using the ALMA archival data. (d) A close-up view of the yellow box in panel (c). Contours are drawn every 3σ with the lowest contour of 3σ. The 1σ level of 0.04 mJy beam^{-1}. The synthesized beam drawn in the bottom right corner has a size of $0\farcs17 \times 0\farcs14$ with a P.A. of $+18\fdg3$. Dashed open circle delineates the nucleus area with a radius of $0\farcs6$ from the continuum peak.

Table 2
Parameters of the Nucleus

Wavelength	Position		S_{peak}	S_{int}	Deconvolved Size			Mass[a]	Mean Density[b]
	α_{ICRS}	δ_{ICRS}	mJy beam^{-1}	mJy	major($''$)	minor($''$)	P.A. ($^\circ$)	$M_\odot$	$\times10^8$ cm^{-3}
1.3 mm	05 35 21.058	−05 00 58.445	1.25 ± 0.06	13.5	1.34	0.82	−82.2	0.089	3.11
1.1 mm	05 35 21.058	−05 00 58.422	0.89 ± 0.03	21.4	0.91	0.60	−82.0	0.085	8.53

Notes.
[a] Dust mass opacity values were assumed to be 0.011 cm^{2}g^{-1} for 1.3 mm and 0.0145 cm^{2}g^{-1} for 1.1 mm.
[b] The effective radii are assumed to be 200 au in 1.3 mm and 150 au in 1.1 mm, which are the geometrical means of the semimajor and semiminor axes.

nucleus. The DCO^+ emission is also associated with MMS3, but not with the northern peak.

The H_2CO emission is detected above 3σ only in the $3_{0,3}$–$2_{0,2}$ transition with $E_{up} = 20.96$ K. The spatially extended H_2CO emission is seen in the northern and western parts of the field of view. The H_2CO emission is bright in MMS3, while it is not detected in the northern peak. The H_2CO emission also comes from the region of the continuum filament. The intensity distribution is an oval-shaped ring surrounding the continuum filament. Such a ring-like distribution in the H_2CO emission is also observed in the well-studied prestellar core, L1544 (Chacón-Tanarro et al. 2019). The H_2CO does not peak toward the nucleus, but shows two local peaks in the vicinity of the nucleus. The brighter one is at $\sim1''$ west, and the fainter one is

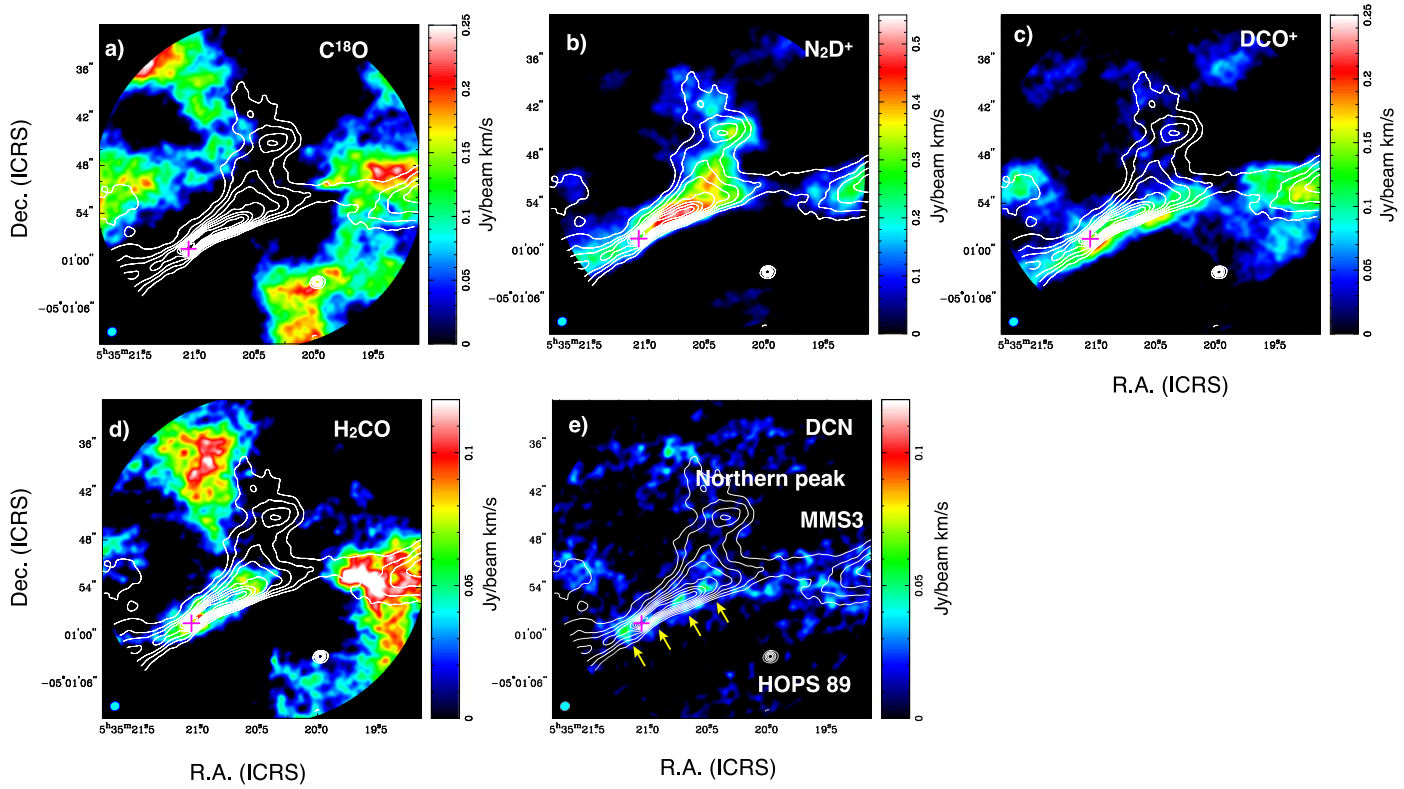

Figure 3. Integrated intensity images of (a) $C^{18}O$ 2–1, (b) N_2D^+ 3–2, (c) DCO^+ 3–2, (d) H_2CO $3_{0,3}$–$2_{0,2}$, (e) DCN 3–2 in color overlaid on the tapered 1.3 mm continuum images drawn in contours. Contours of the 1.3 mm continuum image are drawn every 10% level of the peak flux density. Magenta cross denotes the position of the nucleus. Yellow arrows in panel (e) indicate the positions of the DCN emission spots.

at $\sim 0\farcs5$ east of the nucleus (the detailed distribution of H_2CO in the vicinity of the nucleus is described in Section 6.2). The locations of the two emission peaks are close to but do not coincide with that of the nucleus. The other transitions, $3_{2,2}$–$2_{2,1}$ and $3_{2,1}$–$2_{2,0}$, with higher energy levels of $E_{\rm up} = 68$ K were not detected above the 3σ level.

DCN shows four emission spots at 5σ level along the continuum filament. The positions of the emission spots are indicated by the yellow arrows in Figure 3(e). The DCN emission, the maximum integrated flux density of which is $\sim$0.06 Jy beam^{-1} km s^{-1}, is much fainter than those of the other Deuterated molecules, DCO^+ ($\sim$0.20 Jy beam^{-1} km s^{-1}) and N_2D^+ ($\sim$0.52 Jy beam^{-1} km s^{-1}). This is probably because of the low gas temperature in G208-N2. In contrast to the N_2D^+ and DCO^+, which are formed by H_2D^+ in the temperature range of $<$30 K (Millar et al. 1989), DCN is predominantly formed from CH_2D^+ in the warmer temperature range of 30–70 K (Millar et al. 1989; Turner 2001). DCN is not entirely absent, because a smaller fraction (22%) of DCN can be formed from H_2D^+ in low temperature (Turner 2001).

3.3. Outflow Tracers

In order to search for any outflow associated with the nucleus, the spatial distribution of the CO 2–1 emission was examined. Figure 4 presents the spatial distributions of the blueshifted and redshifted CO emission observed with ALMASOP. The left panels of Figures 4(a) and (c) are the tapered images at $\sim 1''$ resolution, and the right panels ((b) and (d)) are the close-up view of the images without UV taper ($\sim 0\farcs4$ resolution). The blueshifted CO emission extends to the south and west of the triangle-shaped continuum emission, while the redshifted CO is bright in the two elongated features along the north–south direction. As shown in Figure 4(d), there is no redshifted CO emission in the vicinity of the nucleus. On the other hand, the spatially extended blueshifted CO emission is observed in the eastern part of G208-N2 including the nucleus. However, this blueshifted emission is not localized to the nucleus.

The CO emission was also examined using the archival data with higher spectral resolution of 0.32 km s^{-1}. The channel map of CO is shown in Figures A1 and A2 in Appendix A. Although the CO emission in the velocity range from $V_{\rm LSR} \sim 6$—7.5 km s^{-1} extends to the south of the nucleus, this component is likely to be the part of the extended CO emission along the line of sight rather than the outflow from the nucleus.

We also examined the SiO emission, which often traces the shocks associated with outflows, and confirmed that there is no SiO emission in the field of view of G208-N2. Thus, we find no direct evidence of an outflow emanating from the nucleus.

3.4. N_2D^+ Emission with High Spectral Resolution

In order to study the kinematics and physical properties of the dense gas, the high spectral resolution data of N_2D^+ were examined. The channel map of N_2D^+ at 0.1 km s^{-1} resolution and that compared with the channel map of $C^{18}O$ are shown in Figures A3 and A4, respectively, in Appendix. The channel map of $C^{18}O$ (Figure A4) confirms that the $C^{18}O$ emission avoids the region of the filament in all velocity channels. In the velocity range of 11.4–11.8 km s^{-1}, there is a faint $C^{18}O$ emission to the south of the nucleus.

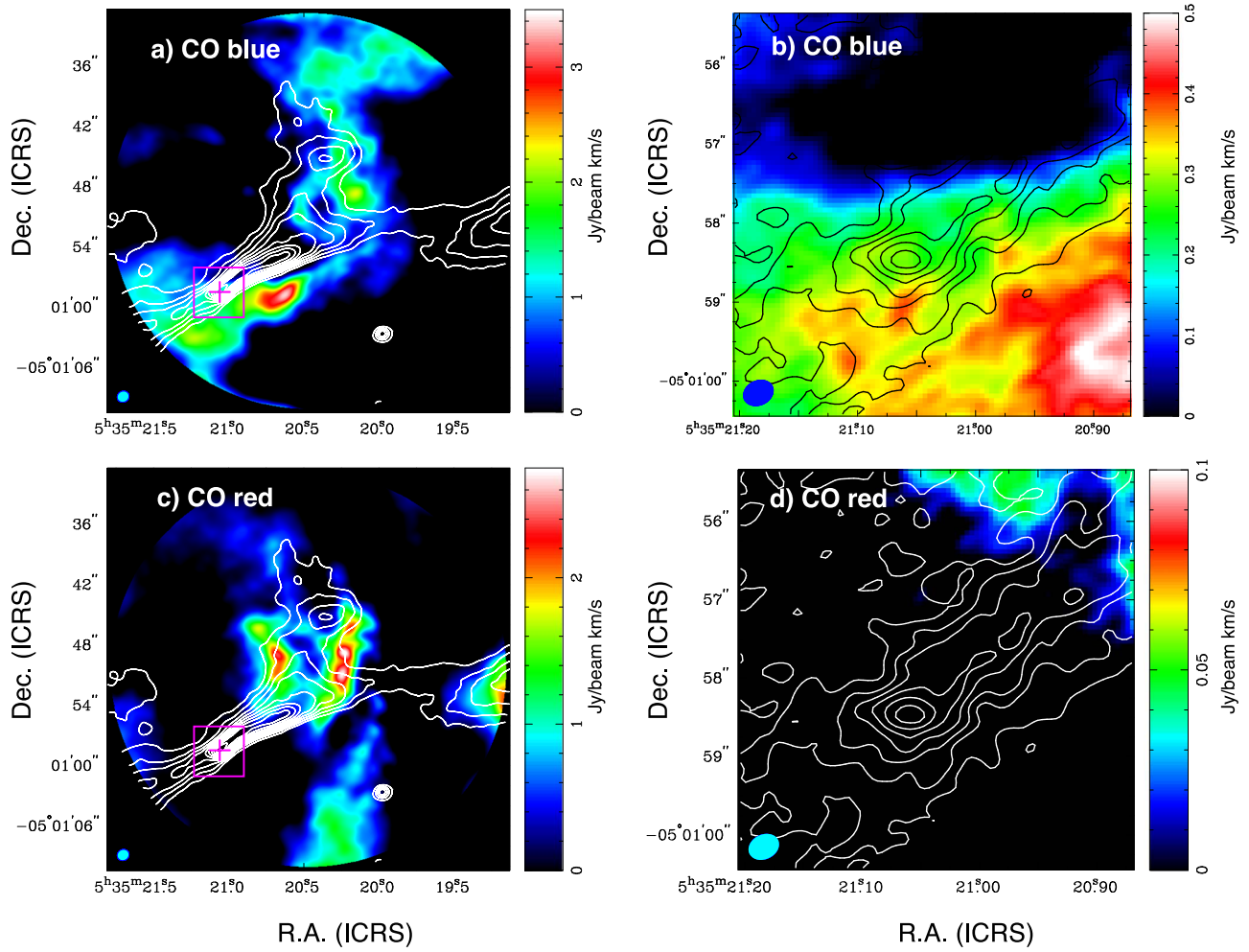

Figure 4. Integrated intensity images of CO 2–1 (color) overlaid on the 1.3 mm continuum images drawn in contours. The velocity ranges of the blueshifted emission (panels (a) and (b)) is $v_{\rm LSR}$ = 0.17–10.33 km s^{-1}, and that of the redshifted emission (panels (c) and (d)) is $v_{\rm LSR}$ = 12.23–16.04 km s^{-1}. Panels (a) and (c) show the tapered CO and continuum images at $\sim$1″ resolution. Contours of the 1.3 mm continuum image are drawn every 10% of the peak flux density. Magenta cross and box denote the position of the nucleus and the area of the close-up view (panels (b) and (d)), respectively. Panels (b) and (d) show the images without UV taper in the small region around the nucleus. Contours of the 1.3 mm continuum image are drawn every 3σ with the 1σ level of 0.084 mJy beam^{-1}.

3.4.1. Hyperfine Spectral Fitting

Since the N_2D^+ 3–2 line consists of numerous hf components, the line parameters such as LSR velocity ($V_{\rm LSR}$), line width ($\Delta V_{\rm FWHM}$), optical depth (τ), and excitation temperature ($T_{\rm ex}$) can be determined from hf fitting. All the hf components are assumed to have the same excitation temperature and line width. The rest frequency and relative intensity of each hf component were referred to in the CDMS catalog (Müller et al. 2001, 2005).

Figure 5 shows the line profiles and the fitting results toward the nucleus and several representative positions along the major and minor axes of the filament through the nucleus. The N_2D^+ 3–2 line consists of three groups of hf components, low-V hf group (7.4–8.0 km s^{-1}), main-V hf group (10.2–12.0 km s^{-1}), and high-V hf group (13.2–13.7 km s^{-1}). The low-V and high-V hf groups, which are often referred to as the satellite hf groups, are clearly seen in most of the region. If the relative strengths of the hf components follow statistical equilibrium, the low-V and high-V hf groups only account for 3.37% and 3.73%, respectively, of the total line strength. The observed integrated intensity of each hf group, however, is $\sim$10% of the total integrated intensity. This implies that the optical depth of the N_2D^+ line is significant, especially in the western part of the continuum filament. Although the bright satellite hf groups could be attributed to non–LTE excitation anomalies as in the case of N_2H^+ (Daniel et al. 2006), such a non–LTE excitation becomes significant for the case of large optical depth. The line parameters toward the nucleus derived from the hf spectral fitting are $T_{\rm ex} = 11.0 \pm 0.4$ K, $\tau_{\rm tot} = 9.1 \pm 1.8$, $V_{\rm LSR} = 10.92 \pm 0.02$ km s^{-1}, and $\Delta V_{\rm FWHM} = 0.29 \pm 0.03$ km s^{-1}.

The spatial distributions of the excitation temperature, optical depth, LSR velocity, and line width derived from the hf spectral fitting are presented in Figure 6. The excitation temperature $T_{\rm ex}$ ranges from $\sim$8 to $\sim$15 K with the average value of $\sim$11 K (Figure 6(a)). The excitation temperature remains relatively stable at around 11–12 K within the continuum filament encompassing the nucleus, but experiences a slight increase by a few kelvins in the northeastern, southeastern, and southern peripheries. The enhanced excitation temperatures observed in these peripheral areas are likely attributed to external heating influences. As shown in the $C^{18}O$ channel map (Figure A4), the diffuse $C^{18}O$ emission is extended in the northeastern region of the filamentary cloud, suggesting the presence of gas with >20 K in this area. The northeastern periphery of the filamentary cloud corresponds to

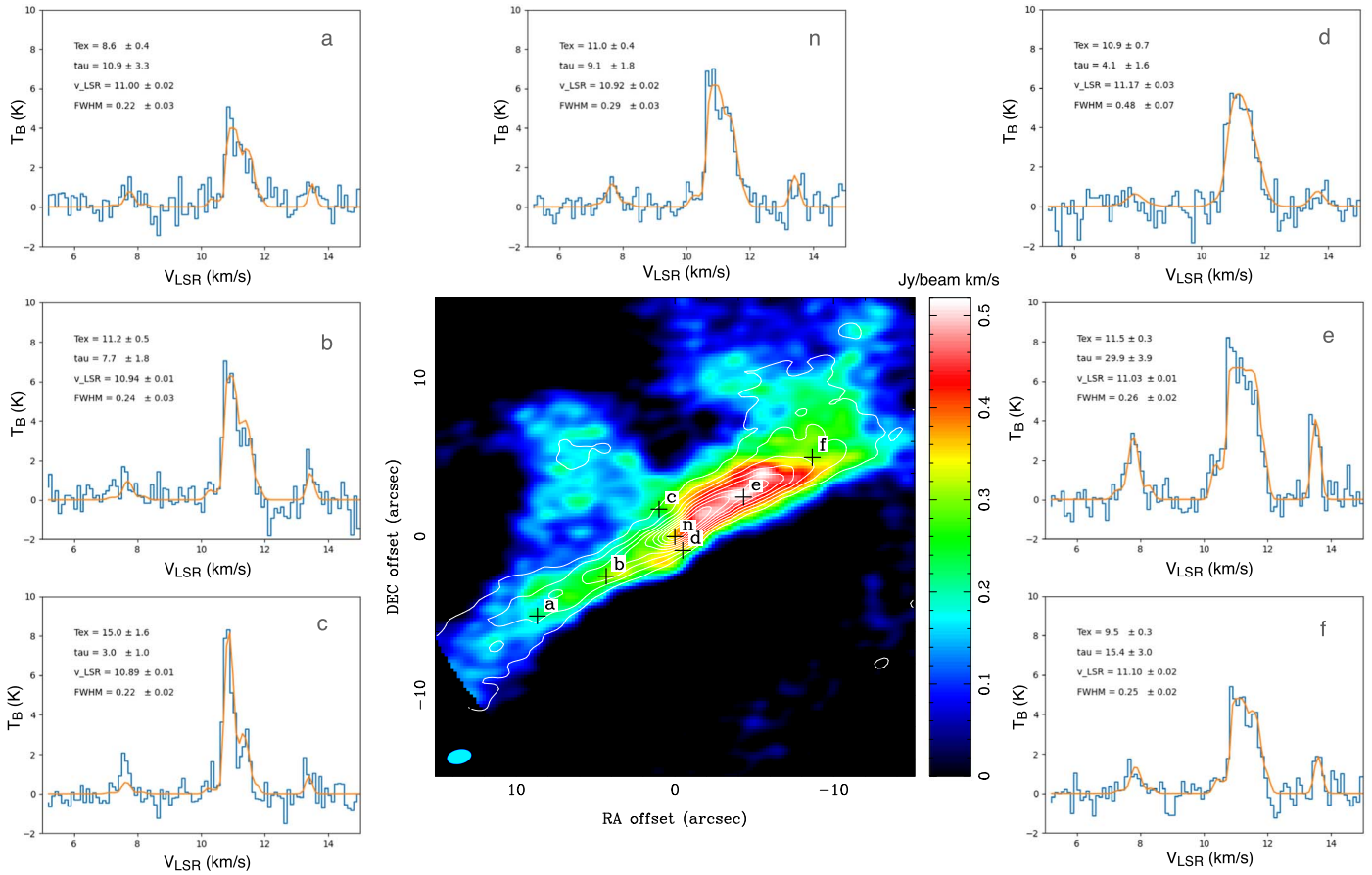

Figure 5. N_2D^+ 3–2 spectra at seven representative positions marked in the moment 0 image in color. Red curves are the results of the hyperfine spectral fitting. The parameters derived from the fitting, excitation temperature, total optical depth, LSR velocity, and the line width in FWHM are given in each panel. 1.3 mm continuum intensity is overlaid on the moment 0 image as white contours. Contours are drawn every 10% level of the peak intensity. The origin of the map is the position of the nucleus (marked as "*n*").

the area where the dense gas is facing the diffuse warmer gas traced by the $C^{18}O$ emission. The elevated excitation temperatures observed in the southeastern and southern peripheries are likely the result of external pressure from the south (see Section 3.4.2).

Figure 6(b) shows that the optical depth of the N_2D^+ emission $\tau_{\rm tot}$ is extremely large (>10) in the filament traced by the continuum emission; especially, $\tau_{\rm tot}$ is higher than 30 in the northwestern part of the filament. This is partly because of the calculation error due to the non-Gaussian line profiles with broad redshifted wings that mimic the flat-topped profiles of the optically thick lines (e.g., Figure 5(e)). However, the bright satellite hf groups suggest that the optical depth of the line is significant in the filament including the nucleus.

The LSR velocity (Figure 6(c)) shows the velocity gradient along the northeast–southwest direction, which is along the minor axis of G208-N2. The overall velocity gradient seen in the N_2D^+ is consistent with that of the large-scale single-dish N_2H^+ 1–0 data, in which redshifted emission with $> 11.2\,{\rm km\,s^{-1}}$ appears to the northeastern and southwestern sides of G208-N2 with a velocity gradient along its minor axis (Luo et al. 2022). Note that the redshifted velocity (>11.3 km s^{-1}) at the southern edge is due to the redshifted wing shown in Figure 5. The velocity also varies along the major axis; the LSR velocity of ∼11.0–11.1 km s^{-1} in the northwestern and southeastern regions decreases to the most blueshifted velocity of ∼10.8 km s^{-1} in the vicinity of the nucleus. In addition, the LSR velocity changes significantly across the nucleus from $V_{\rm LSR} \sim 10.8\,{\rm km\,s^{-1}}$ in the northeast to ∼11.2 km s^{-1} in the southwest.

The line width (Figure 6(d)) tends to be enhanced (> 0.3 km s^{-1}) along the southern edge of the continuum filament due to the redshifted wing emission. On the other hand, it is rather narrow (<0.25 km s^{-1}) in the northern part of the continuum filament where the effect of the redshifted wing emission is negligible. The nonthermal velocity dispersion $\Delta v_{\rm nt}$ is derived by

$$\Delta v_{\rm nt} = \left[\frac{(\Delta v'_{\rm FWHM})^2}{8\ln 2} - \frac{kT_{\rm kin}}{\mu(N_2D^+)}\right]^{1/2}, \quad (2)$$

where $\Delta v'_{\rm FWHM}$ is the line width obtained from the hf spectral fitting after the correction of the spectral resolution. Here, k is the Boltzman constant, $T_{\rm kin}$ is the gas kinetic temperature, and μ is the molecular mass. Assuming that the gas kinetic temperature is ∼11 K, the nonthermal velocity dispersion is calculated to be $< 0.08\,{\rm km\,s^{-1}}$, which is smaller than the sound speed,

$$c_{\rm s} = \left[\frac{kT_{\rm kin}}{\mu_p m_{\rm H}}\right]^{1/2}, \quad (3)$$

where μ_p is the mean molecular mass per free particle, 2.37; and $m_{\rm H}$ is the mass of atomic hydrogen. Using the same

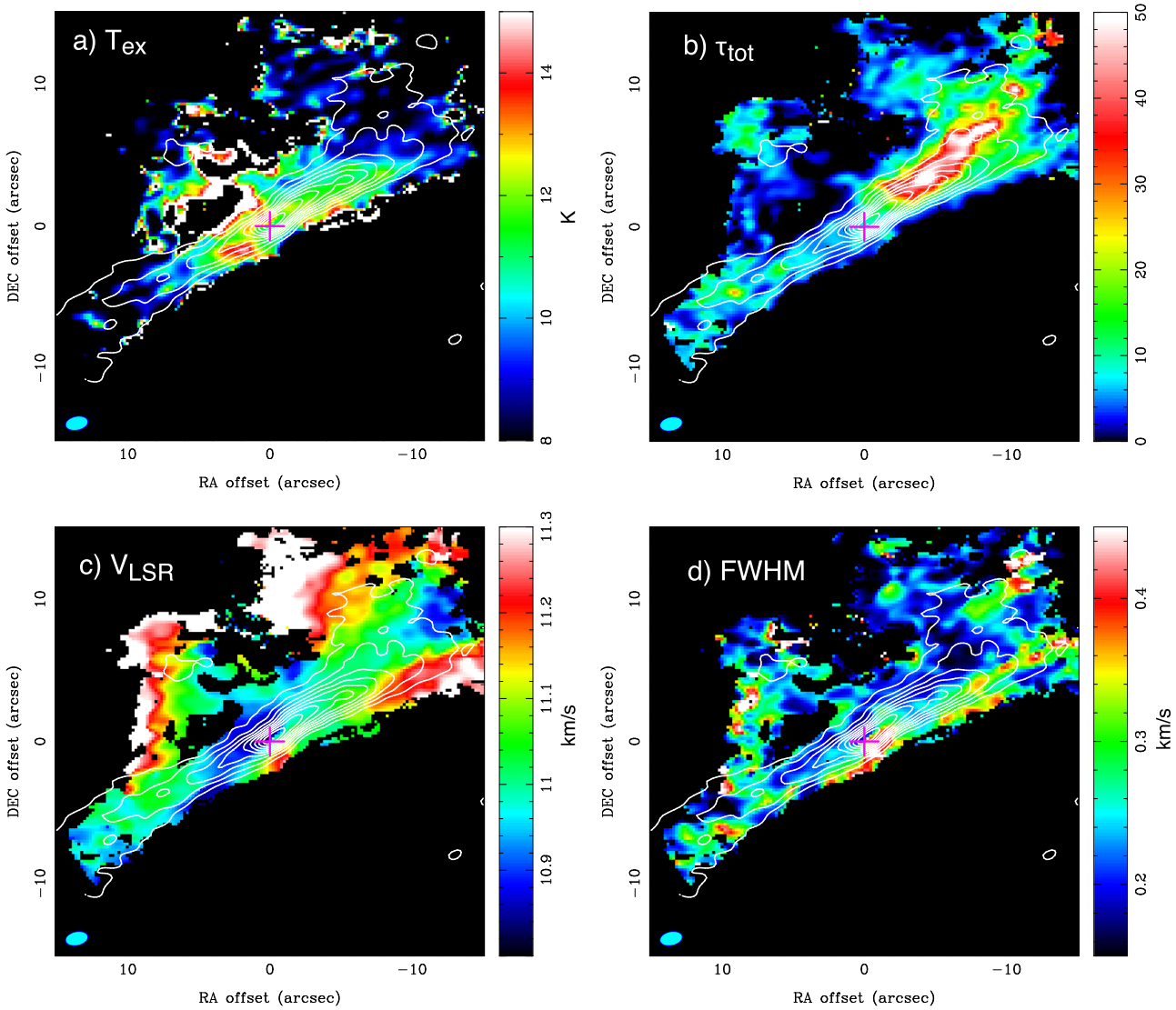

Figure 6. Line parameters for N_2D^+ 3–2 derived from the hyperfine fitting in color, (a) excitation temperature, (b) total optical depth, (c) LSR velocity, and (d) line width. 1.3 mm continuum emission observed in 2015.1.00341.S is overlaid as contours. Contours are drawn every 1.563 mJy beam^{-1}, which corresponds to the 10% level of the peak intensity. The origin of the map is the position of the nucleus (magenta cross).

temperature, c_s is 0.20 km s^{-1}. This implies that the turbulent velocity of the gas in the continuum filament is subsonic.

3.4.2. Kinematics of the Dense Gas

Figures 7(a) and (b) show the position–velocity (PV) diagrams of N_2D^+ along the major and minor axes, respectively, of the filament through the nucleus. Figure 7(a) reveals that the N_2D^+ line intensity drops sharply on the blue side, while it decreases gradually on the red side. The enhancement of the wing on the red side is significant in the western part of the filament. There are small velocity gradients that decrease toward the nucleus from both sides. The velocity gradients are ∼0.3 and ∼0.2 km s^{-1} per 12″ in the eastern side and the western side, respectively (the cyan lines in Figure 7(a)). These velocity gradients correspond to 13.2 and 8.8 km s^{-1} pc^{-1}, respectively. On the other hand, the velocity structure along the minor axis (Figure 7(b)) exhibits a pronounced *V*-shaped pattern. The velocity gradually decreases from $V_{\rm LSR} \sim 11.27$ km s^{-1} at 10″ north to ∼10.73 km s^{-1} at the nucleus. This velocity gradient corresponds to 28.5 km s^{-1} pc^{-1}. Then, the broad redshifted wing appears suddenly at the southern edge, toward which the line intensity drops sharply. This implies that the dense gas is compressed by the external pressure from the southwest. Figure 7(c) shows that the redshifted wing is extended over the filament, suggesting that the gas in the filament is highly perturbed by the external pressure. The nucleus is located at the boundary of the perturbed and quiescent regions. The significant velocity change across the nucleus shown in Figure 6(c) is due to this redshifted perturbed component.

4. Analysis

4.1. H_2 Column Density

The column density of molecular hydrogen can be estimated using the 1.3 mm continuum emission by the following formula:

$$N(\mathrm{H_2}) = \frac{S_\nu}{\Omega_{\rm m}\mu m_{\rm H}\kappa_\nu B_\nu(T_{\rm dust})}, \quad (4)$$

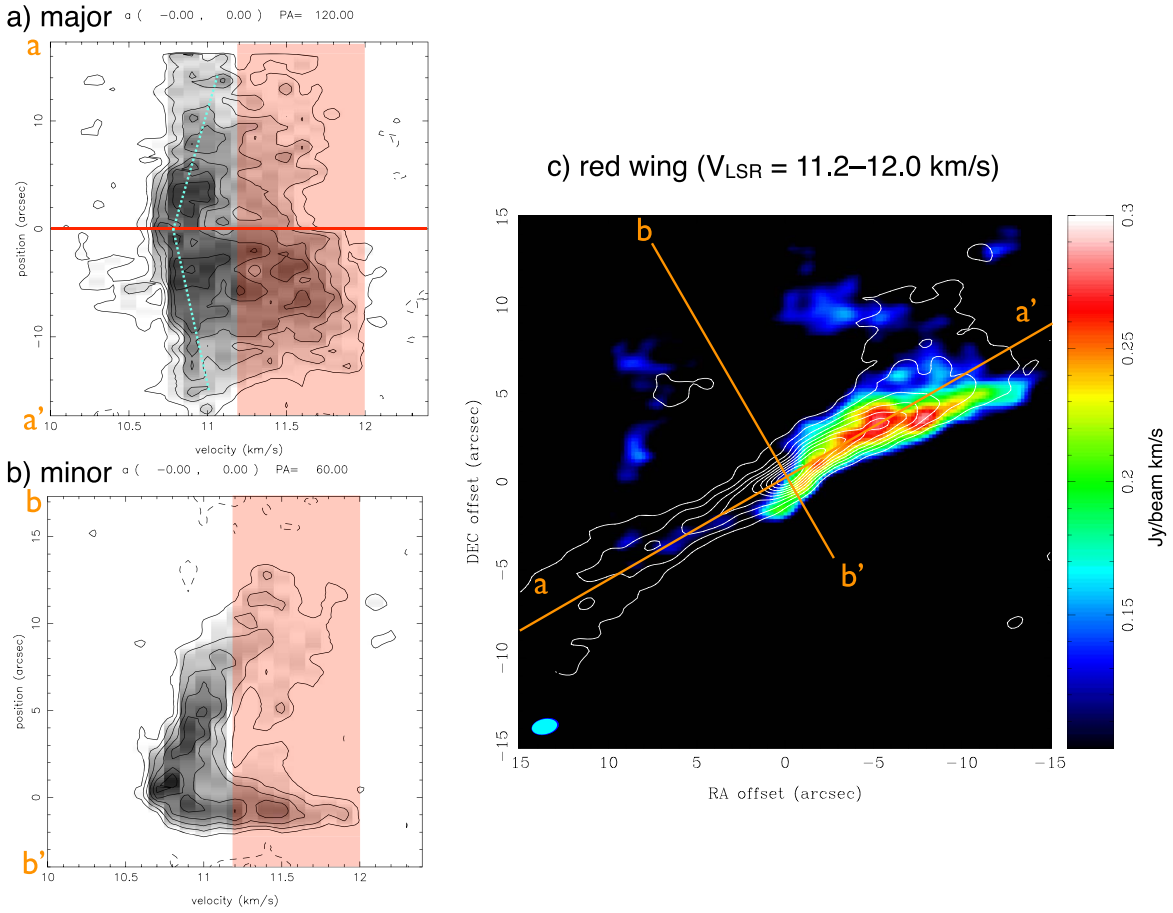

Figure 7. Position–velocity diagrams of N_2D^+ along the (a) major (a–a′) and (b) minor (b–b′) axes of the filament through the nucleus. The orange horizontal line and shaded area in each panel denote the location of the nucleus and the velocity range of the red wing (V_{LSR}=11.2–12.0 km s^{-1}), respectively. The cyan dotted lines in panel (a) represent the velocity gradients along the major axis. (c) Red wing of the N_2D^+ in color overlaid on the 1.3 mm continuum in white contours. Orange lines (a–a′ and b–b′) are the cuts of the *P*–*V* diagrams.

where S_ν is the flux density, Ω_m is the solid angle of the beam, μ is the mean molecular weight, i.e., 2.8, m_H is the mass of the atomic hydrogen, κ_ν is the dust mass opacity, and $B_\nu(T_{dust})$ is the Planck function at a temperature of T_{dust}. We adopt the theoretical dust opacity of $\kappa_{230\,GHz} = 0.0106$ cm^{2}g^{-1} for the MRN size distribution with thin ice mantles at a number density of 10^7 cm^{-3} (Ossenkopf & Henning 1994). The gas-to-dust ratio is assumed to be 100. Here, the dust temperature is assumed to be same as the excitation temperature of N_2D^+ derived from the hf fitting. Since the excitation temperature of N_2D^+ agrees well with the kinetic temperature derived from NH_3 (Li et al. 2013), this assumption should be reasonable for the region where the gas and dust temperatures are coupled.

The derived H_2 column density distribution is shown in Figure 8(a). Since 1.3 mm continuum emission is optically thin, the H_2 column density distribution follows the intensity distribution of the continuum emission. The H_2 column density exceeds 5×10^{23} cm^{-2} in the area of the continuum filament. The mass of the continuum filament (including the nucleus) is 0.59 $M_\odot$. Assuming the cylindrical geometry with a diameter of 1.″5 (590 au), the mean density of the continuum filament is calculated to be 5.9×10^7 cm^{-3}. The H_2 column density toward the position of the nucleus is estimated to be $(8.4 \pm 0.2) \times 10^{23}$ cm^{-2}.

4.2. N_2D^+ Column Density

The column densities of N_2D^+ have been calculated using the excitation temperatures (T_{ex}) and optical depths (τ_{tot}) derived from the hf fitting. The N_2D^+ emission is optically thick in the entire area of G208-N2, especially where τ_{tot} is larger than 10 in the filament including the nucleus. Therefore, the column density was estimated using the integrated intensities of the low-*V* and high-*V* hf groups following the method described in Bourke et al. (2012). Most of the optical depth of the N_2D^+ line is due to the main-*V* hf group, the contribution of which is 0.929 to the total line intensity (normalized to 1.0). On the other hand, the contributions of the low-*V* and high-*V* hf groups to the total line intensity are 0.0373 and 0.0337, respectively. Therefore, the emission of these satellite groups is considered to be optically thin except for the area with extremely large τ_{tot} of > 30. We used the integrated intensities of the low-*V* (7.4–8.0 km s^{-1}) and high-*V* (13.2–13.7 km s^{-1}) hf groups and assumed that the emission is optically thin. Then, the derived column density was scaled by the inverse of the relative line intensity, $1/(0.0373+0.0337)$.

The column density of N_2D^+, $N(N_2D^+)$, derived in this method is shown Figure 8(b). The $N(N_2D^+)$ is higher than 5×10^{12} cm^{-2} in the entire region of G208-N2, with values higher than 2×10^{13} cm^{-2} in the northwestern part with large optical depth. The N_2D^+ column density values derived here

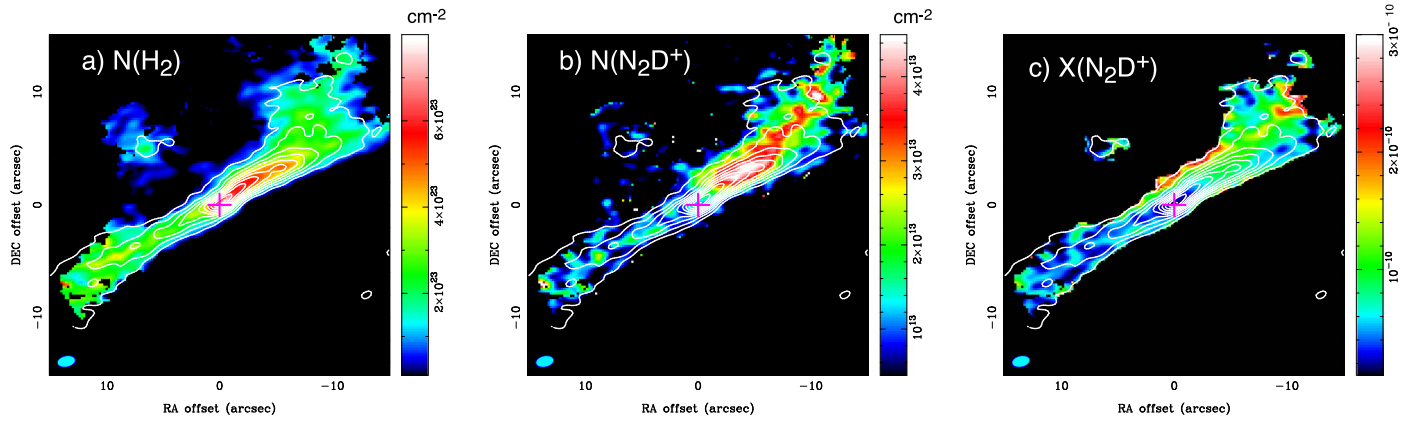

Figure 8. (a) H_2 column density derived from the 1.3 mm continuum emission, assuming the dust temperature same as the excitation temperature of N_2D^+. The range of the color scale is from 1.0×10^{22} to 8.0×10^{23} cm^{-2}. (b) Column density of N_2D^+ derived from the integrated intensity of the satellite hf groups scaled by the inverse of the relative line intensity, 1/(0.0373+0.0337). The range of the color scale is from 4.5×10^{12} to 4.5×10^{13} cm^{-2}. (c) Fractional abundance of N_2D^+ derived from column densities of H_2 (a) and N_2D^+ (b). The range of the color scale is from 1.0×10^{-11} to 3.0×10^{-10}. 1.3 mm continuum emission observed in 2015.1.00341.S is overlaid as white contours. Contours are drawn every 1.563 mJy beam^{-1}, which corresponds to the 10% level of the peak intensity. The origin of the map is the position of the nucleus (magenta cross).

are consistent with $(7.5 \pm 0.7) \times 10^{12}$ cm^{-2} derived from the $J = 1$–0 transition observed with the NRO 45 m telescope (Kim et al. 2020). The $N(N_2D^+)$ toward the nucleus is estimated to be $(1.3 \pm 0.3) \times 10^{13}$ cm^{-2}. Here, the error on $N(N_2D^+)$ is estimated from the rms noise level of the integrated intensity (Caselli et al. 2002). The highest value of $\sim 4.5 \times 10^{13}$ cm^{-2} is obtained at $\sim 4\farcs3$ northwest of the nucleus.

The $N(N_2D^+)$ values derived from the satellite hf groups are compared with those derived from the total integrated intensities (including the main-V hf group) and total optical depths, $\tau_{\rm tot}$, in the eastern part with $\tau_{\rm tot} < 10$. The values derived from the satellite groups are lower by a factor of ~ 2 as compared to those derived from the total integrated intensity and $\tau_{\rm tot}$. This implies that the $N(N_2D^+)$ shown in Figure 8(b) could be underestimated, even though the derived values of $> 2 \times 10^{13}$ cm^{-2} are ~ 10 times higher than the N_2D^+ column densities measured in the nearby low-mass star-forming regions such as ρ-Oph A-N6 (Bourke et al. 2012) and B1-bN/B1-BS (Huang & Hirano 2013).

4.3. N_2D^+ Abundance

The fractional abundance of N_2D^+, $X(N_2D^+)$ was derived from the column densities of N_2D^+ and H_2, and presented in Figure 8(c). The $X(N_2D^+)$ is enhanced to $> 10^{-10}$ in the northwestern part because of the high $N(N_2D^+)$ of $> 2 \times 10^{13}$ cm^{-2} and moderate $N(H_2)$ of $\sim 2 \times 10^{23}$ cm^{-2}. The $X(N_2D^+)$ is $\sim 8 \times 10^{-11}$ in the western part of the filament, and decreases to $< 2 \times 10^{-11}$ in the vicinity of the nucleus, toward which the N_2D^+ abundance shows the local minimum. The $X(N_2D^+)$ at the position of the nucleus is derived to be $(1.6 \pm 0.4) \times 10^{-11}$ cm^{-2}, which is 1 order of magnitude lower than the highest value in the northwestern region.

5. Physical Properties of the Filament and Nucleus

5.1. Physical Properties of the Filament

Using the mean density of the continuum filament derived in Section 4.1, the line mass of the continuum filament, $M_{\rm line}$, is calculated to be $M_{\rm line} \sim 1.67 \times 10^{16}$ g cm^{-1} ($=5.9\ M_\odot$ pc^{-1}). On the other hand, the critical line mass for an infinite filament in hydrostatic equilibrium is calculated by Stodólkiewicz (1963), Ostriker (1964):

$$M_{\rm crit} = \frac{2\Delta v_{\rm tot}^2}{G}, \quad (5)$$

where $\Delta v_{\rm tot}$ is a total velocity dispersion including both thermal and nonthermal contributions, and G is the gravitational constant. The total velocity dispersion, $\Delta v_{\rm tot}$, is

$$\Delta v_{\rm tot} = [\Delta v_{\rm nt}^2 + c_s^2]^{1/2}. \quad (6)$$

The typical line width, $\Delta v_{\rm FWHM}$, measured in the northern part of the continuum filament with less affected by the redshifted wing is ~ 0.25 km s^{-1}. The nonthermal dispersion calculated by Equation (2) is 0.08 km s^{-1}, and the total velocity dispersion calculated by Equation (6) is 0.21 km s^{-1} for $T_{\rm kin} = 11$ K. The critical line mass is calculated to be $M_{\rm crit} = 1.3 \times 10^{16}$ g cm^{-1} ($=20.5\ M_\odot$ pc^{-1}). The $M_{\rm line}/M_{\rm crit}$ is ~ 1.26, implying that the filament is close to the critical state between stable and unstable.

If the magnetic field is taken into account, the critical line mass can be larger. The critical line mass including the contribution of the magnetic field can be calculated using the formula described in Li et al. (2022a). The magnetic field strength in the dense clump including G208-N2 was estimated to be ~ 0.78 mG assuming that the OMC-3 ridge lies close to the plane of the sky (Li et al. 2022b). If the magnetic field strength in the continuum filament is comparable to that in the larger scale clump, i.e., the filament is formed through the contraction along the magnetic field that is roughly perpendicular to the OMC-3 ridge (Matthews et al. 2001; Houde et al. 2004; Li et al. 2022b), the contribution of the magnetic field to the critical line mass is negligible. If the magnetic field strength is comparable to that observed in the protostellar envelopes, i.e., a few to 5 mG (Girart et al. 2006; Hull et al. 2017; Aso et al. 2021), the critical line mass becomes larger by a factor of ~ 1.5. These imply that the magnetic field does not affect the dynamical state of the continuum filament significantly.

5.2. Radial Density Profile of the Nucleus

Figure 9(a) shows the H_2 column density of the nucleus as a function of the distance from the peak. The column density was

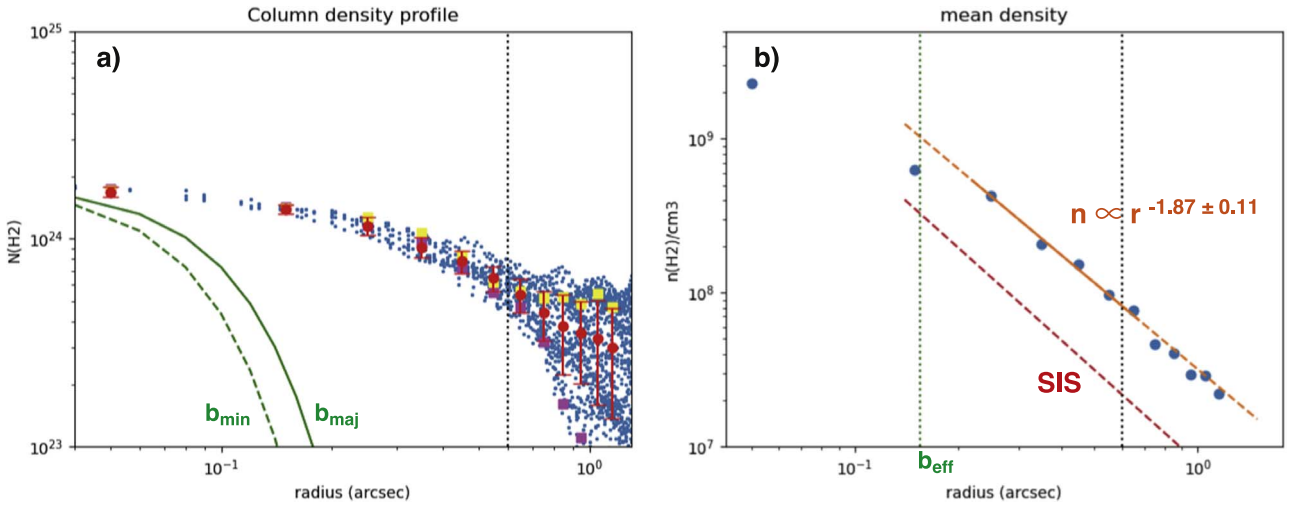

Figure 9. (a) Radial profile of the H_2 column density for the nucleus derived from the 1.1 mm continuum emission. The red dots with error bars are the azimuthal average of $N(H_2)$ at 0.″1 bins. The yellow and magenta squares are the H_2 column density profiles along the position angles of 120° and 30°, respectively. The green solid and dashed curves denote the synthesized beam along the major and minor axes, respectively. (b) Radial number density profile of the nucleus assuming spherical symmetry. The orange line shows the best-fit power-law profile to the data points at radii larger than the effective beam size (dotted vertical line). The red line shows the density profile for the SIS (r^{-2}) with an effective sound speed of 0.21 km s^{-1}.

derived using the 1.1 mm continuum data, which achieved the highest angular resolution of ∼0.″15, allowing the nucleus to be spatially resolved. In order to minimize contamination due to the emission from the filament, the pixels in the eastern half of the nucleus (with the position angles from 30° to 210°) were used for the analysis. The dust temperature was assumed to be constant at $T_{\rm dust} = 11$ K, which is derived from the hf fitting of the N_2D^+ observed at ∼1.″2 resolution. The dust mass opacity, $\kappa_{260\ \rm GHz}$, was adopted to be 0.0145 cm^{2}g^{-1} for the gas density of 10^8 cm^{-3} (Ossenkopf & Henning 1994).

Assuming that the nucleus is spherically symmetric and consists of concentric shells, the radial density profile was derived from the column density profile. First, the column densities are azimuthally averaged in each radial bin with a 0.″1 width (the red dots in Figure 9(a)). Then, the mass in each annulus is calculated from the averaged column density and the area of the annulus. The mass enclosed within a radius r is derived by summing up the masses of the annuli inside r. The mean volume density in each shell is determined from the mass of annulus divided by the volume of the shell with the same radius and width of the corresponding annulus. Figure 9(b) shows the mean density as a function of radius. The volume density increases from $\sim 10^8$ cm^{-3} at $r = 0.''6$ (230 au) to $\sim 2 \times 10^9$ cm^{-3} at the center. The density profile at $r > 0.''2$ (80 au) is fit by a power law with an index of -1.87 ± 0.11 (orange solid line in Figure 9(b)), which is close to $r^{-2.0}$. It should be noted that the deviation from spherical symmetry is significant at $r > 0.''7$ because of the filamentary distribution of the continuum emission. The column density along the filament (yellow squares in Figure 9(a)) does not decrease at $r > 0.''7$ due to the low-level continuum emission that extends to the east of the nucleus, while the column density across the filament drops sharply (magenta squares in Figure 9(a)). Therefore, the data points at $r > 0.''7$ were not used for the power-law fitting because the mean density values in the outer area are not reliably dominated by the nucleus. The innermost two data points locate below the $r^{-1.87}$ line, implying the possible density flattening at the center. However, due to the limited angular resolution of ∼0.″15, it is difficult to determine the density profile at $r < 0.''2$ region. Although the density profile of the nucleus, $r^{-1.87}$, is close to that of the SIS with $\rho(r) = (\Delta v_{\rm tot}^2/2\pi G) r^{-2}$, where $\Delta v_{\rm tot}$ is an effective sound speed (Shu 1977), and the density scaling is not consistent with that of a SIS. Given the line width toward the nucleus obtained from the hf spectral fitting, which is 0.29 km s^{-1}, the total velocity dispersion derived by the Equation (6) becomes 0.22 km s^{-1}. The density profile of the SIS utilizing this $\Delta v_{\rm tot}$ is shown in the red dashed line in Figure 9(b). It is evident that the density of the nucleus at each radius is higher than that of the SIS value by a factor of ∼3.7. This implies that the gravity is stronger than thermal and turbulent pressure at every radii in the nucleus.

It should be noted that the assumed gas temperature, which is derived from the hf spectral fitting of N_2D^+ observed at lower resolution, does not always represent the gas temperature in the nucleus. If the temperature in the nucleus decreases toward the small radius as in the case of L1544 (Crapsi et al. 2007), the actual density profile could be steeper than the derived value. If the nucleus is collapsing dynamically, the isothermal condition can be maintained by the continuous inflow of the gas from the outer region. On the other hand, if the nucleus contains an internal heating source, the temperature could exceed 11 K. In such a case, the density profile in the central region becomes flatter.

The virial parameter of the nucleus in the absence of magnetic support is calculated by

$$\alpha = \frac{5R\Delta v_{\rm tot}^2}{aGM}, \tag{7}$$

where R is a radius of the nucleus, $\Delta v_{\rm tot}$ is a total 1D velocity dispersion derived from Equation (6), a is a constant that depends on the density distribution, G is the gravitational constant, and M is the mass of the nucleus (Bertoldi & McKee 1992). The constant a is given as $a = (1 - n/3)/(1 - 2n/5)$ for the case of the power-law density profile of $\propto r^{-n}$, and is 5/3 for $n = 2$. The radius of the nucleus was assumed to be $r = 0.''6$ (230 au; dashed open circle in Figure 2(d)), within which the contamination of the filament component is less significant. The mass enclosed in a radius of

230 au (0.″6) is estimated to be ∼0.1 $M_{\odot}$. Utilizing the total velocity dispersion in the nucleus, which is 0.22 km s^{-1}, the virial parameter α is calculated to be 0.39, which implies that the nucleus cannot be supported by turbulence.

Kauffmann et al. (2013) argued that the cores with low virial parameters are not collapsing. The velocity dispersions in the collapsing cores should increase due to the inward motions, resulting in the virial parameter α to be closer to 2a (i.e., $10/3$ for $n = 2$). The N_2D^+ line does not exhibit the signature of such line broadening toward the nucleus. The absence of line broadening in N_2D^+ may be attributed to the inability of this line to trace the gas in the vicinity of the nucleus due to molecular depletion. As described in Section 4.3, the N_2D^+ abundance decreases toward the nucleus, suggesting that this molecule disappears from the gas in the immediate vicinity of the nucleus.

On the other hand, the nucleus could be supported against a collapse by magnetic field. The maximum mass, M_{Φ}, supported by magnetic field can be calculated by

$$M_{\Phi} = c_{\Phi}\frac{\pi BR^2}{G^{1/2}}, \quad (8)$$

where B is the magnetic field strength, and c_{Φ} is 0.09 for a centrally condensed cloud (Tomisaka et al. 1988). Using Equation (8), the required field strength to support the nucleus with a mass of ∼0.1 $M_{\odot}$ and a radius of 230 au is estimated to be ∼15 mG. Even though the contribution of the turbulence is taken into account, a very strong field of ∼10 mG is required to support the nucleus. The field strength measured for typical protostellar envelopes with a mean density of a few times 10^7 cm^{-3} is on the order of a few mG (Girart et al. 2006; Hull et al. 2017; Aso et al. 2021). Under the flux-freezing condition, the scaling relation between the magnetic field strength and density is $B \propto \rho^{1/2}$ (Crutcher 2012; Tritsis et al. 2015; Hennebelle & Inutsuka 2019). Therefore, the field strength can be $\gtrsim$10 mG in a region with a mean density of a few times 10^8 cm^{-3} if the magnetic field is frozen in the matter.

6. Discussion

6.1. Chemical Stratification in G208-N2

As shown in Sahu et al. (2021), the spatial distribution of the N_2D^+ emission shows good correlation with that of the continuum emission. However, the column density of N_2D^+ exhibits significantly different distribution with respect to the H_2 column density due to the presence of the high opacity component in the northwestern part of the filament. This implies that G208-N2 consists of two components; one is the continuum filament harboring the nucleus (filament component), and the other is the one with high N_2D^+ column density (N_2D^+ abundant component) located to the northwestern part. Although two components are not clearly identified in the channel map of N_2D^+ (Figure A3) due to the blending of the multiple hf components, the radial velocity distribution (Figure 6(c)) suggests that these two components have slightly different radial velocities, i.e., $V_{\rm LSR} \sim 10.8$–10.9 km s^{-1} in the filament component and $V_{\rm LSR} \sim 11.0$–11.1 km s^{-1} in the N_2D^+abundant component. The $X(N_2D^+)$ value of the N_2D^+ abundant component is higher than $>10^{-10}$, which is comparable to the fractional abundance of N_2H^+, 3.0×10^{-10}, in dense cores (Caselli et al. 2002). The N_2D^+ abundance in the western part of the filament component is not clear because this part spatially overlaps with the N_2D^+ abundant component. The N_2D^+ abundance drops significantly to $<2 \times 10^{-11}$ in the vicinity of the nucleus. The possible origin of this abundance drop is discussed in the next subsection.

As described in Section 3.2, the $C^{18}O$ emission is completely missing in the dense gas of G208-N2. Since the total power (TP) data are not combined, the missing $C^{18}O$ flux should be significant. However, the missing $C^{18}O$ flux mainly comes from the spatially extended component along the line of sight, which is not associated with the dense gas in this core. If the extended $C^{18}O$ emission along the line of sight has a large optical depth, it could obscure the emission from the G208-N2 core. In order to estimate the optical depth of the extended $C^{18}O$ emission, we used the spectra obtained with the TP array having a beam size of ∼30″. As shown in Figure B1, the brightness temperature of the $C^{18}O$ spectrum observed toward the nucleus position is ∼8.8 K, while that of the ^{12}CO spectrum is ∼26 K. Assuming that the excitation temperature of the extended $C^{18}O$ emission, $T_{\rm ex}(C^{18}O_{\rm fg})$, is the same as the peak brightness temperature of the ^{12}CO emission, the optical depth of the extended $C^{18}O$ emission, $\tau(C^{18}O_{\rm fg})$, is estimated to be ∼0.55. If it is the case, the foreground $C^{18}O$ emission does not completely obscures the emission from the G208-N2 core. On the other hand, $\tau(C^{18}O_{\rm fg})$ becomes larger than unity for $T_{\rm ex}(C^{18}O_{\rm fg}) < 19$ K. If $T_{\rm ex}(C^{18}O_{\rm fg})$ is comparable to that of the dense gas, i.e., ∼15 K, the foreground cloud with $\tau(C^{18}O_{\rm fg}) \sim 2$ obscures ∼90% of the emission from the dense core behind it. This scenario can explain the absence of $C^{18}O$ emission from the G208-N2 core. Nevertheless, such an extended foreground component with large optical depth might obscure the $C^{18}O$ emission from the neighboring protostellar cores, MMS3 and MMS5, located at ∼33″ and ∼26″ distances from the nucleus. Given the $C^{18}O$ flux densities observed in MMS3 and MMS5 that correspond to the brightness temperatures of ∼10 and ∼15 K, respectively (Matsushita et al. 2019; Morii et al. 2021), it is unlikely that a substantial portion of the emission from these cores is obscured.

It is more plausible that the lack of $C^{18}O$ emission within the dense gas of G208-N2 is attributable to substantial CO depletion. The 3σ upper limit of the $C^{18}O$ intensity is estimated to be ∼90 mJy beam^{-1}, which corresponds to ∼1.58 K in the brightness temperature unit. Assuming that the $C^{18}O$ emission has the same line width as N_2D^+, i.e., ∼0.3 km s^{-1}, the upper limit of the integrated intensity becomes 0.48 K km s^{-1}. Under the LTE condition with an excitation temperature of 11 K, and the optically thin line emission, the column density of $C^{18}O$ is calculated to be $N(C^{18}O) < 2.8 \times 10^{14}$ cm^{-2}. Since the H_2 column density derived from the 1.3 mm continuum emission is higher than 2×10^{23} cm^{-2} in the entire region of G208-N2, the upper limit of the $C^{18}O$ abundance, $X(C^{18}O)$, is estimated to be $\sim 10^{-9}$. The derived $C^{18}O$ abundance is more than 2 orders of magnitude lower than the $C^{18}O$ abundance value often used in the interstellar medium, $(1.7$–$2)\times 10^{-7}$ (Wannier 1980; Frerking et al. 1982). This implies that the $C^{18}O$ (CO) depletion factor in G208-N2 is greater than 100 in the entire region, which is 1 order of magnitude larger than those of the nearby prestellar cores in the same size scale (Crapsi et al. 2005). The $C^{18}O$ (CO) depletion factor toward the nucleus is even higher, and is >350.

The DCO^+ emission is enhanced at the southern edge of the triangle-shaped dense gas. Since DCO^+ formation requires CO

in the gas phase through the reactions of $H_2D^+ + CO \rightarrow DCO^+ + H_2$ and $N_2D^+ + CO \rightarrow DCO^+ + N_2$, the enhanced DCO^+ emission implies that the southern edge of the dense gas is heated above the sublimation temperature of CO, ~25 K. The faint $C^{18}O$ emission is seen in the velocity range from $V_{LSR} = 11.3$–11.8 km s^{-1} in the channel map (Figure A4). The location of this component is consistent with that of the DCO^+ emission shown in Figure 3(c).

The oval-shaped morphology of the H_2CO emission suggests that H_2CO traces the external layer surrounding the continuum filament. H_2CO can be formed through both grain-surface chemistry and gas-phase chemistry. In the gas-phase route, H_2CO is formed through reactions of hydrocarbons such as CH_2 and CH_3 with oxygen atoms (Yamamoto 2017). In the case of the G208-N2, this route is unlikely because carbon is completely locked to CO and frozen onto the grain surface in such a dense and cold environment. In the region where CO is frozen out, H_2CO is formed on the grain surfaces by successive hydrogenation of CO. The H_2CO in the ice can be released in the gas phase when the grains are heated to its sublimation temperature. However, the sublimation temperature of H_2CO is ~40 K for the desorption energy of 2050 K (Garrod & Herbst 2006), which is much higher than the gas temperature in G208-N2. UV-induced photodesorption is also unlikely, because UV radiation cannot reach the surface of the continuum filament. Possible desorption mechanisms in the external layer could be grain heating by means of the impact of cosmic rays (Herbst & Cuppen 2006) or the formation energy released by the exothermic reaction (Garrod et al. 2006).

6.2. Local Gas Heating in the Vicinity of the Nucleus

As shown in Figure 8(c) and Figure 10(a), the N_2D^+ abundance that is $\sim 8 \times 10^{-11}$ in the western part of the filament decreases by a factor of ~5 in the vicinity of the nucleus. Since the density of the gas in the vicinity of the nucleus is extremely high, $>10^7$ cm^{-3}, N_2, a parent molecule of N_2D^+, is expected to freeze-out if the temperature is low. The binding energy of N_2 measured in the laboratory experiments is ~0.9 times of that of CO (Öberg et al. 2005; Fayolle et al. 2016). As a result, the N_2 freeze-out temperature is a few degrees lower than that of CO. Although the clear anticorrelation between $C^{18}O$ and N_2D^+ observed in G208-N2 implies that the N_2 freeze-out timescale is longer than that of CO, N_2 could also freeze-out in the region of the highest density. In the center of the well-studied prestellar core, L1544, the temperature of which decreases toward the center (Crapsi et al. 2007), the depletion of N_2D^+ and other N-bearing deuterated species, NH_2D, is observationally confirmed (Redaelli et al 2019; Caselli et al. 2022). Therefore, if there is no heating source embedded in the nucleus, the temperature drop and N_2 depletion could also happen in the nucleus of G208-N2.

Alternatively, the N_2D^+ abundance decreases in the vicinity of the nucleus because of the increased temperature due to the embedded heating source. Although the nucleus is not detected in the wave bands shorter than 70μm (Figure 1), this does not exclude the presence of embedded heating source. One of the first hydrostatic core (FHSC) candidates B1-bN is also not detected in these wave bands (Pezzuto et al. 2012). Once the central source is formed, small amount of CO starts to sublimate, destroy N_2D^+, and decrease the N_2D^+ abundance. Although the $C^{18}O$ emission is not detected toward the nucleus, this does not completely rule out the presence of small amount of CO in the gas phase. The upper limit of the CO abundance toward the nucleus derived from that of the $C^{18}O$ abundance is $<3 \times 10^{-7}$, assuming the O^{16}/O^{18} of 560 (Wilson & Rood 1994). This is much larger than the N_2D^+ abundance, 1.6×10^{-11} at the nucleus and $\sim 10^{-10}$ in the region with high N_2D^+ abundance. This scenario also explains the presence of the two H_2CO emission spots in the vicinity of the nucleus. As shown in Figure 10(b), two H_2CO emission spots, one at 1.″25 (490 au) northwest and the other at 0.″5 (200 au) east of the nucleus, are located in the region with low N_2D^+ abundance. These H_2CO emission spots could be the signposts of the warm regions.

In the case of the thermal desorption of H_2CO due to the radiation from the central object, the H_2CO emission is expected to appear toward the nucleus. Since the nucleus does

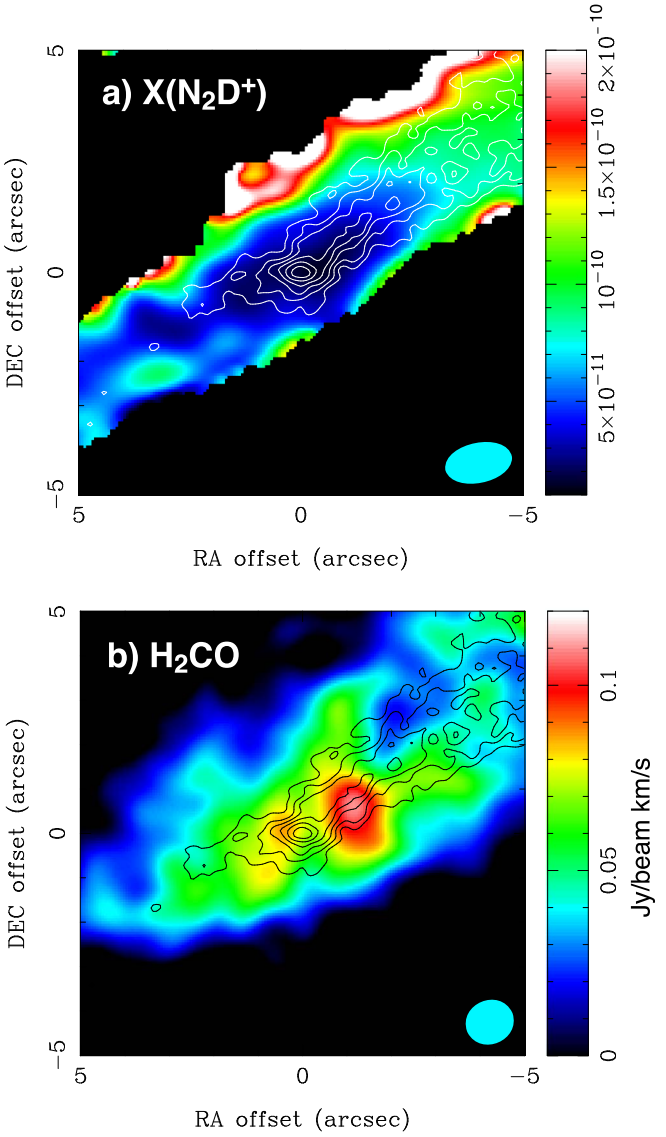

Figure 10. (a) Fractional abundance of N_2D^+ and (b) integrated intensity of H_2CO $3_{0,3}$–$2_{0,2}$ in the vicinity of the nucleus overlaid on the 1.3 mm continuum images drawn in contours. The contours are drawn every 3σ with the lowest contour level of 6σ. The 1σ level is 0.084 mJy beam^{-1}. The beam size of the 1.3 mm continuum is 0.″38 × 0.″30, while those of the N_2D^+ and H_2CO shown in the bottom right of each panel are 1.″53 × 0.″91 and 1.″10 × 1.″03, respectively.

not have a counterpart in the Herschel 70 μm image, the luminosity of the putative central object should be very low. The upper limit flux of the nucleus at 70 μm derived from the rms noise level is ∼60 mJy. The upper limit of the internal luminosity of the nucleus can be roughly estimated using the empirical relation between $L_{\rm int}$ and 70 μm flux (Dunham et al. 2008). Using this method, the upper limit of the internal luminosity of the nucleus is estimated to be 0.03 $L_\odot$. The sublimation radius of H_2CO is expected to be ∼20–30 au for such a very-low luminosity object (Aikawa et al. 2008). However, neither of the H_2CO peaks coincides with the position of the nucleus. If the envelope surrounding the nucleus has cavities as in the cases of the envelopes in Class 0 protostars, the radiation from the central object can rather freely escape through the cavity. Even so, it is very difficult for the very-low luminosity source to heat the large area of 200–500 au to the sublimation temperature of H_2CO.

Instead of the thermal desorption, the H_2CO could be sublimated by means of slow shocks. The two H_2CO peaks offset from the nucleus could be the outflow lobes as in the cases of the outflows from the youngest protostars, B1-bN and B1-bS (Gerin et al. 2015). Since the outflows traced by the H_2CO emission are ∼5″ (∼1500 au) in B1-bN and ∼10″ (∼3000 au) in B1-bS, the 200–500 au offsets of the H_2CO peaks can be explained if they are tracing the compact outflow lobes from the central object. The caveat to this scenario is the absence of the CO counterpart. However, this could be due to the very low velocity of this putative outflow. Since the H_2CO emission is detected only in the single channel with a velocity resolution of 1.55 km s^{-1}, the radial velocity of the putative outflow is <0.8 km s^{-1}. Such a low-velocity *outflow* could be completely overwhelmed by the CO emission from the cloud, which is resolved out by the interferometer. Another possible scenario is the slow shocks resultant from the inflow. The velocity gradient along the major axis (Figure 7(a)) reveals a gradual reduction in LSR velocities of the gas on either side of the nucleus. Such a *V*-shaped configuration centered on the nucleus can be attributed to the inflow of gas toward the nucleus, with the filamentary structure potentially undergoing a kink and inclination shift at the same location. The H_2CO emission spot is brighter in the western side, as the shock is stronger due to the inflow of higher-density gas. In order to study the nature of the H_2CO emission spots, high spectral resolution observations of H_2CO are necessary.

6.3. Evolutionary Stage of the Nucleus

The nucleus in G208-N2 has a radius of ∼230 au and a mass of ∼0.1 $M_\odot$. The nucleus has a very high central density of $\sim 2 \times 10^9$ cm^{-3}. Although the radial density profile, $r^{-1.87}$, is close to r^{-2} for the SIS, the density at each radius is higher than that of the SIS by a factor of ∼3.7. The stability analysis implies that the nucleus is gravitationally unstable unless it is supported by a strong magnetic field of >10 mG. The central density of the nucleus in G208-N2, i.e., $\sim 10^9$ cm^{-3}, is comparable to that of SM1N in Ophiuchus A (Friesen et al. 2018), although the nucleus in G208-N2 is 3 times more massive than that of SM1N. In the case of Oph A SM1N, the flatter density profile of $r^{-1.3}$ and the detection of the blueshifted and redshifted CO emission with a velocity extent of a few kilometers per second imply the presence of the central embedded object, which is FHSC or early Class 0 stage (Friesen et al. 2018). If the two emission spots seen in the H_2CO image are indeed indicators of the outflow, the nucleus may harbor its central source. The upper limit of its internal luminosity derived from the upper limit 70 μm flux is 0.03 $L_\odot$, which is in the range of the FHSC predicted from the theoretical models, $L \lesssim 0.25$–$0.1\ L_\odot$ (e.g., Omukai 2007; Saigo et al. 2008; Commerçon et al. 2012; Vaytet et al. 2012). The mass of the nucleus, ∼0.1 $M_\odot$, is not large enough to form a low-mass star unless the entire gas in the nucleus is converted into a star. This implies the possibility that the central putative source could evolve into a brown dwarf. However, the small velocity gradients along the filament from the both sides of the nucleus suggest that the nucleus can acquire additional gas from the filament and form a low-mass star. Conversely, if the H_2CO emission spots result from inflow shocks, the nucleus has not yet formed its central object. In this case, the nucleus can be in the prestellar stage on the verge of FHSC formation.

6.4. Shock Compression

The *P*–*V* diagram of N_2D^+ across the filament (Figure 7(b)) exhibits a *V*-shaped pattern with broad redshifted wing emission at the southern edge where the line intensity drops sharply. This implies that the dense gas in G208-N2 is compressed by the external pressure from the south. The enhancement of the DCO^+ emission at the southern boundary also supports the presence of shocks that heat the gas above the sublimation temperature of CO. Furthermore, the continuum filament, characterized by an average density of 10^7 cm^{-3}, exhibits a parallel alignment with the southern periphery of the dense gas traced by the N_2D^+ line. This also suggests that external pressure from the south compressed the dense gas within G208-N2, leading to the formation of a denser filament within. However, the origin of this external pressure is unclear. The northern part of OMC-3, in which G208-N2 is embedded, resides along the southwestern periphery of the expanding bubble delineated by the [C II] emission driven by NGC 1977 (Pabst et al. 2020), suggesting that this filamentary cloud was formed under the influence of the pressure from the bubble. Nevertheless, the pressure exerted by this bubble originates from the northeastern direction, contrasting with the pressure coming from the south. It is also unlikely that the pressure localized to G208-N2 originates from such a gigantic bubble with a radius of 1.6 pc. There is a flat spectrum YSO HOPS 89 (Megeath et al. 2012; Furlan et al. 2016) at ∼17″ southwest of the nucleus. However, this YSO does not show any signature of outflow that can account for the external pressure. The Class 0 protostar HOPS 88 (Megeath et al. 2012; Furlan et al. 2016) embedded in the neighboring core MMS5 is driving a bipolar outflow along the east–west direction (Aso et al. 2000; Williams et al. 2003; Takahashi et al. 2008). Although the western lobe of this outflow overlaps with the location of G208-N2, this lobe is blueshifted with respect to the cloud systemic velocity. Therefore, this outflow is unlikely to be the origin of the external pressure that produces the redshifted N_2D^+ wing emission. The moment 1 map of ^{13}CO 1–0 (Kong et al. 2018) reveals that the dense gas in OMC-3 having a radial velocity of ∼10.5–11.0 km s^{-1} is embedded in the diffuse gas with ∼12 km s^{-1}. Therefore, the origin of the external pressure could be diffuse molecular gas surrounding OMC-3 region.

6.5. End-dominated Collapse in the Filamentary Structure

In the case of the filaments with finite lengths, in which gas motion along the filament becomes important, their collapse is different from that of the filament with infinite length. It is known that collapsing finite-sized filaments form dense condensations at the filament edges by means of gravitational focusing (e.g., Bastien 1983; Burkert & Hartmann 2004; Pon et al. 2012; Clarke & Whitworth 2015). On the basis of analytical calculations of the collapse timescales, Pon et al. (2012) revealed that this end-dominated collapse mode becomes more important with increasing aspect ratio. The dense condensations formed at the ends of the filament can collapse locally before the entire filament converges toward its center when the local collapse timescale is significantly shorter than the global collapse timescale (Pon et al. 2011).

This end-dominated collapse scenario is applicable to both the OMC-3 ridge, in which G208-N2 is embedded, and the continuum filament in G208-N2, in which the nucleus is embedded. The northern part of the OMC-3 ridge from MMS1 to MMS6 with a length of ∼0.35 pc and a width of ∼0.06 pc has an aspect ratio of ∼6. According to Pon et al. (2012), the timescale of the global collapse with an end-dominated mode is $\sqrt{32A/\pi^2}\ \tau_{ff}$, where A is an aspect ratio, and τ_{ff} is a freefall timescale. The freefall timesceale of this ridge with a mean density of $\sim 4 \times 10^5$ cm^{-3} (Schuller et al. 2021) is estimated to be $\sim 4.9 \times 10^4$ yr. Hence, the collapse timescale for the OMC-3 ridge with an aspect ratio of ∼6 becomes $\sim 2.2 \times 10^5$ yr. The timescale for the global collapse could be longer because the magnetic field perpendicular to the OMC-3 ridge (Matthews et al. 2001; Houde et al. 2004; Li et al. 2022b) provides support along the major axis of the ridge. Once the dense condensation with $>10^6$ cm^{-3} is formed at the edge, the freefall timescale of this condensation, $\sim 3.3 \times 10^4$ yr, is much shorter than the global collapse timescale. Therefore, the condensation formed at the end can collapse locally.

On the basis of 1D hydrodynamic simulations, Hanawa et al. (1994) showed that the formation of a dense condensation can propagate along the filament; if the local collapse mode works, the condensation formed at the edge could be isolated from the parent filament. Consequently, the parent filament could have a new edge where a subsequent condensation takes form. If the formation of condensation occurs at both ends of the filament, it propagates inward at approximately the effective sound speed. Takahashi et al. (2013) argued that this model can explain the evolutionary scenario of the OMC-3 ridge, which harbors the youngest condensation, G208-N2, in the middle of the chain of condensations. They estimated the timescale required for the fragmentation to propagate from the two edges of the ridge to G208-N2 at the center to be $\sim 3 \times 10^5$ yr.

Within the G208-N2 core, the compact nucleus is located at the eastern end of the continuum filament. Although the filamentary cloud itself extends to the southeast of the nucleus, the H_2 column density exhibits a significant decrease of ∼50% at ∼1″ (400 au) east of the nucleus. Such a configuration can also be explained in the context of the end-dominated collapse of the finite-sized filament. Hanawa et al. (1994), Pon et al. (2011) examined the formation of condensations at the end of the filament with a gradual density decrease. They found that the end-collapse occurs in the filaments with tapered edges, although the collapse timescale increases as the length of the tapered region increases. The filament in G208-N2 contains only one condensation at its eastern edge instead of two condensations at both edges. The absence of condensation in the western edge of the G208-N2 filament can be explained by the gradual density decrease in the northwest. The numerical simulation of Burkert & Hartmann (2004) also shows that the surface density gradient leads to the formation of a single condensation at the dense end.

The timescale of the end-dominated global collapse of the continuum filament with a mean density of $\sim 5.9 \times 10^7$ cm^{-3} and an aspect ratio of ∼8 is estimated to be $\sim 2.2 \times 10^4$ yr. On the other hand, the freefall timescale of the nucleus with a mean density of $3.1\text{–}8.5 \times 10^8$ cm^{-3} is 1200–2000 yr, which is 1 order of magnitude shorter than that of the continuum filament. Hence, the nucleus can collapse locally and form a protostar within.

The quiescent and extremely dense object, akin to the nucleus in G208-N2, is rarely observed in nearby star-forming regions owing to its extremely short freefall timescale. The presence of such a short-lived object within G208-N2 can be attributed to the filamentary configuration of G208-N2 itself, nestled within the larger scale filamentary structure of the OMC-3 ridge. Due to this filament-in-filament configuration, the collapse timescale of G208-N2 surpasses that of neighboring cores within the OMC-3 ridge. As previously discussed in Section 5.2, the magnetic field strength may prove sufficient to counteract gravitational collapse if the nucleus was formed under the flux-freezing condition.

7. Summary

We have studied the internal structure of the prestellar core G2008-N2 in the OMC-3 region using the ALMA in the 1.3 and 1.1 mm wave bands. The high resolution ALMA images have unveiled an extraordinarily dense nucleus nestled within this filamentary-shaped prestellar core. The main results are summarized as the following:

1. The continuum emission from G208-N2 shows a narrow filamentary structure having a size of 4700 ×590 au with an aspect ratio of ∼8. The position angle of this continuum filament is ∼120°, which is roughly same as that of the OMC-3 ridge. The H_2 column density exceeds 5×10^{23} cm^{-2} in the area of the continuum filament. The mass and mean density of this filament is $\sim 0.59\ M_\odot$ and 5.9×10^7 cm^{-3}, respectively. The line mass of the continuum filament, 1.67×10^{16} g cm^{-1} (=25.9 $M_\odot$), is slightly larger than the critical line mass of the isothermal cylinder at 11 K, suggesting that the filament is close to the critical state between stable and unstable.
2. The continuum filament harbors a compact *nucleus* with a radius of ∼150–200 au and a mass of ∼0.1 $M_\odot$ at its eastern end. The volume density at the center of the nucleus is $\sim 2 \times 10^9$ cm^{-3}. Such a compact and exceedingly dense object has been discovered within the prestellar core for the first time. There is no sign of CO outflow localized to this nucleus.
3. The nucleus has a radial density profile of $r^{-1.87\pm0.11}$. Although this density profile is close to r^{-2} for the SIS, the density scaling is higher than that of the SIS value by a factor of ∼3.7. The virial parameter of the nucleus, determined from the velocity dispersion of the N_2D^+ 3–2 line, is remarkably low at 0.39. These imply that the gravity is dominant over the pressure everywhere in the

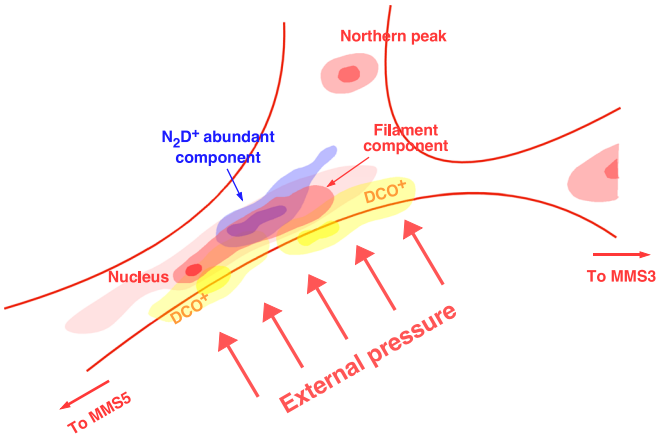

Figure 11. Schematic diagram of G208-N2. The line of sight is perpendicular to the plane.

nucleus unless the nucleus is strongly supported by magnetic field exceeding 10 mG.

4. The molecular line data exhibit significant chemical stratification in G208-N2. The complete absence of $C^{18}O$ emission implies CO depletion in the dense gas of G208-N2. The CO depletion factor is greater than 100 in the entire region, and >350 toward the nucleus. Although the spatial distribution of the N_2D^+ emission shows good correlation with that of the continuum emission, the column density of N_2D^+ is enhanced on the north of the continuum filament. This implies that G208-N2 consists of two components; one is the continuum filament with high H_2 column density, and the other is the one with high N_2D^+ column density. The DCO^+ emission is enhanced at the southern edge of the continuum filament, implying the external heating from the south. A schematic diagram of G208-N2 is given in Figure 11.
5. The redshifted N_2D^+ wing emission and the enhancement of the DCO^+ emission at the southern boundary of the triangle-shaped dense gas suggest that the dense gas is compressed and heated by the shock from the south, although the origin of the external pressure is not identified.
6. The N_2D^+ emission does not peak toward the nucleus. As a result, the N_2D^+ abundance exhibits the local minimum toward the nucleus. This could imply either the depletion of N_2, a parent molecule of N_2D^+, due to low temperature and high density or a limited release of CO from the dust, potentially attributed to the presence of an internal heating source.
7. There are two H_2CO emission spots at ∼200 au east and ∼500 au west of the nucleus, which could be the locations of slow shocks caused by either low-velocity outflow or inflow. If the two emission spots are the signature of low-velocity outflow, the nucleus may harbor its central source, which could be a candidate for the FHSC. Conversely, if the emission spots results from inflow shocks, the nucleus is likely to be in the prestellar stage on the verge of FHSC formation.
8. The nucleus is formed at the end of the continuum filament that is embedded in the middle of the larger scale filamentary structure in the northern part of OMC-3. This implies that the gravitational focusing in the finite-sized filament plays an important role in the evolution of both the OMC-3 ridge and the continuum filament within G208-N2. The presence of the extremely dense nucleus, which is a short-lived object, can be attributed to the filament-in-filament configuration, leading to an evolutionary timescale longer than that of neighboring cores within the OMC-3 ridge.

Acknowledgments

This paper makes use of the following ALMA data: ADS/JAO.ALMA#2015.1.00341.S and #2018.1.00302.S. ALMA is a partnership of ESO (representing its member states), NSF (USA), and NINS (Japan), together with NRC (Canada), NSC and ASIAA (Taiwan), and KASI (Republic of Korea), in cooperation with the Republic of Chile. The Joint ALMA Observatory is operated by ESO, AUI/NRAO, and NAOJ. We thank Dr. A. Trejo for helpful suggestions in data calibration. N.H. acknowledge support from the National Science and Technology Council (NSTC) with grants NSTC 110-2112-M-001-048 and NSTC 111-2112-M-001-060. D.S. acknowledges the support from Ramanujan Fellowship (SERB) and PRL, India. K.T. was supported by JSPS KAKENHI (grant No. JP20H05645). This work has been supported by the National Key R&D Program of China (No. 2022YFA1603100). T.L. and P.S. Li acknowledge the support by National Natural Science Foundation of China (NSFC) through grants No.12122307 and No.12073061, the international partnership program of Chinese Academy of Sciences through grant No.114231KYSB20200009, and Shanghai Pujiang Program 20PJ1415500. D.J. is supported by NRC Canada and by an NSERC Discovery Grant. L.B. gratefully acknowledges support by ANID BASAL project FB210003. H.-L. Liu is supported by Yunnan Fundamental Research Project (grant No. 202301AT070118). C.W.L. is supported by the Basic Science Research Program through the National Research Foundation of Korea (NRF) funded by the Ministry of Education, Science and Technology (NRF-2019R1A2C1010851), and by the Korea Astronomy and Space Science Institute grant funded by the Korea government (MSIT; Project No. 2023-1-84000). The work of M.G.R. is supported by NOIRLab, which is managed by the Association of Universities for Research in Astronomy (AURA) under a cooperative agreement with the National Science Foundation.

Facility: ALMA.

Software: astropy (Astropy Collaboration et al. 2013), CASA (McMullin et al. 2007), Miriad (Sault et al. 1995).

Appendix A
Channel Maps

Figures A1 and A2 show the CO 2–1 channel maps at 0.32 km s^{-1} resolution. The channel map of the N_2D^+ and that of $C^{18}O$ overlaid on the N_2D^+ are shown in Figures A3 and A4, respectively.

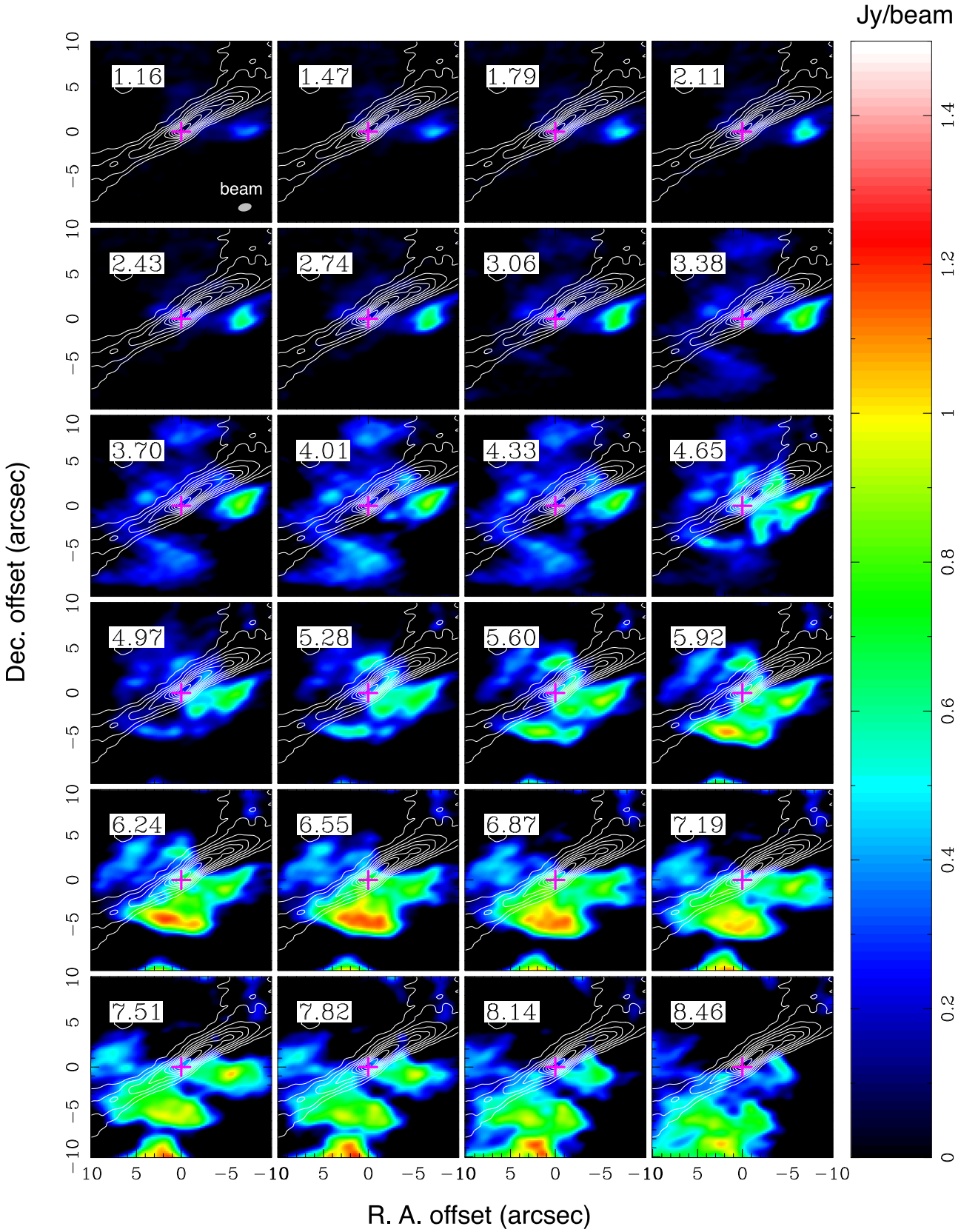

Figure A1. Channel map of the CO 2–1 emission line at 0.32 km s^{-1} resolution in color overlaid on the 1.3 mm continuum image in contours. The velocity range is from 1.16 to 8.46 km s^{-1}. Contours are drawn every 10% level of the pdak flux density. The magenta cross denotes the position of the nucleus.

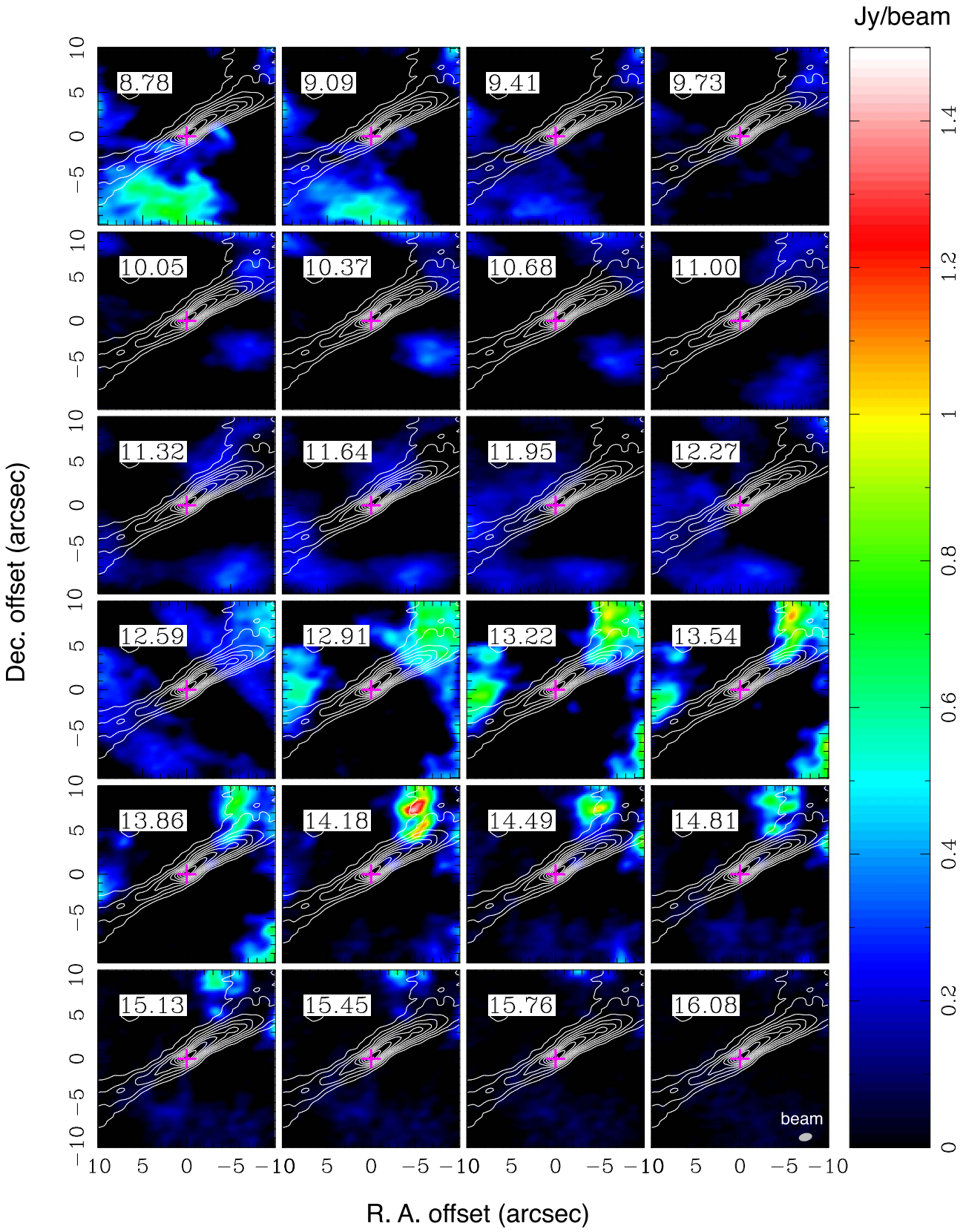

Figure A2. Channel map of the CO 2–1 from $V_{\rm LSR} = 8.78$ to 16.08 km s^{-1}.

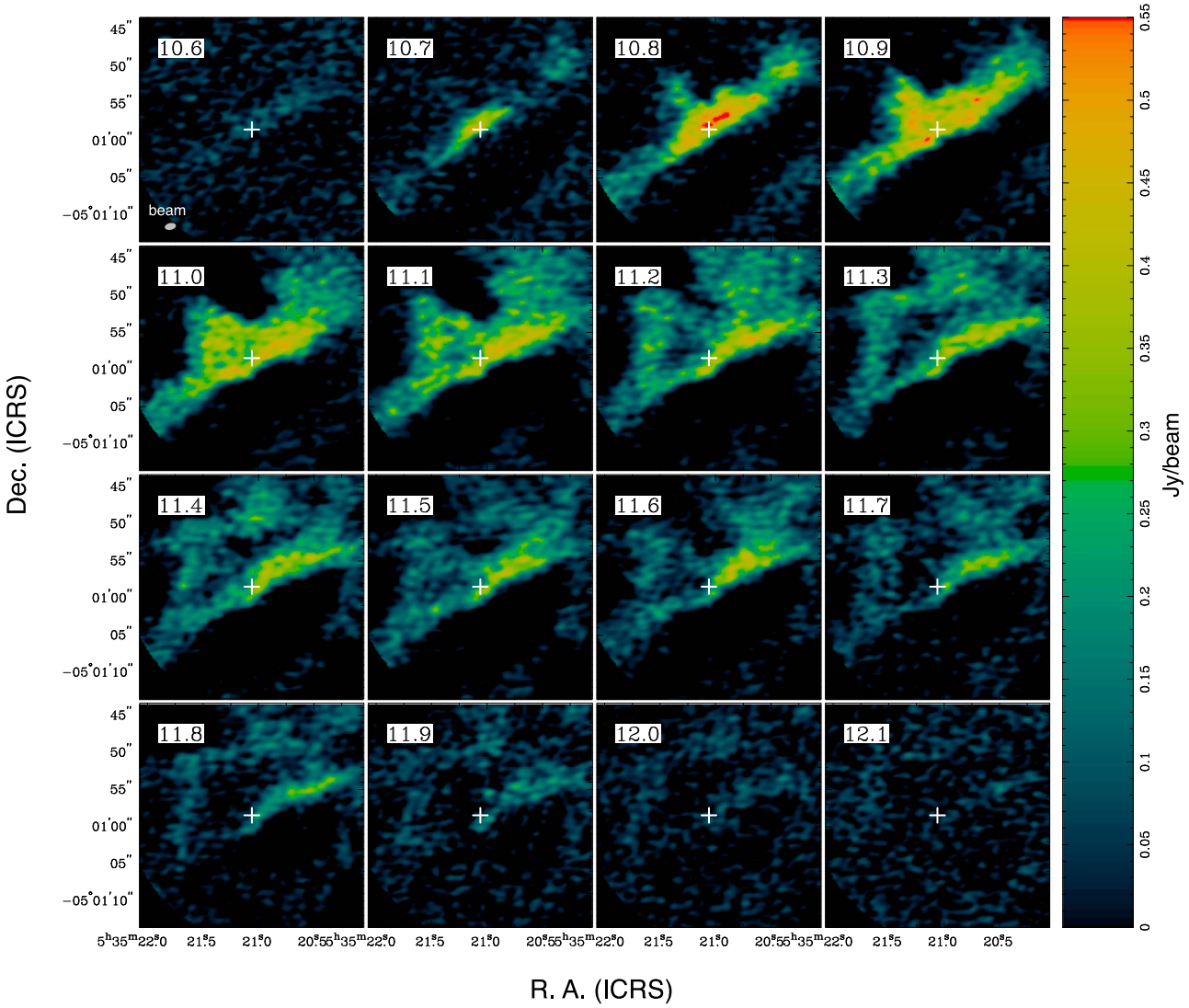

Figure A3. Channel map of the N_2D^+ 3–2 emission line. The velocity resolution in 0.1 km s^{-1}. The LSR velocity refers to the rest frequency of 231.32187 GHz. The white cross denotes the position of the nucleus.

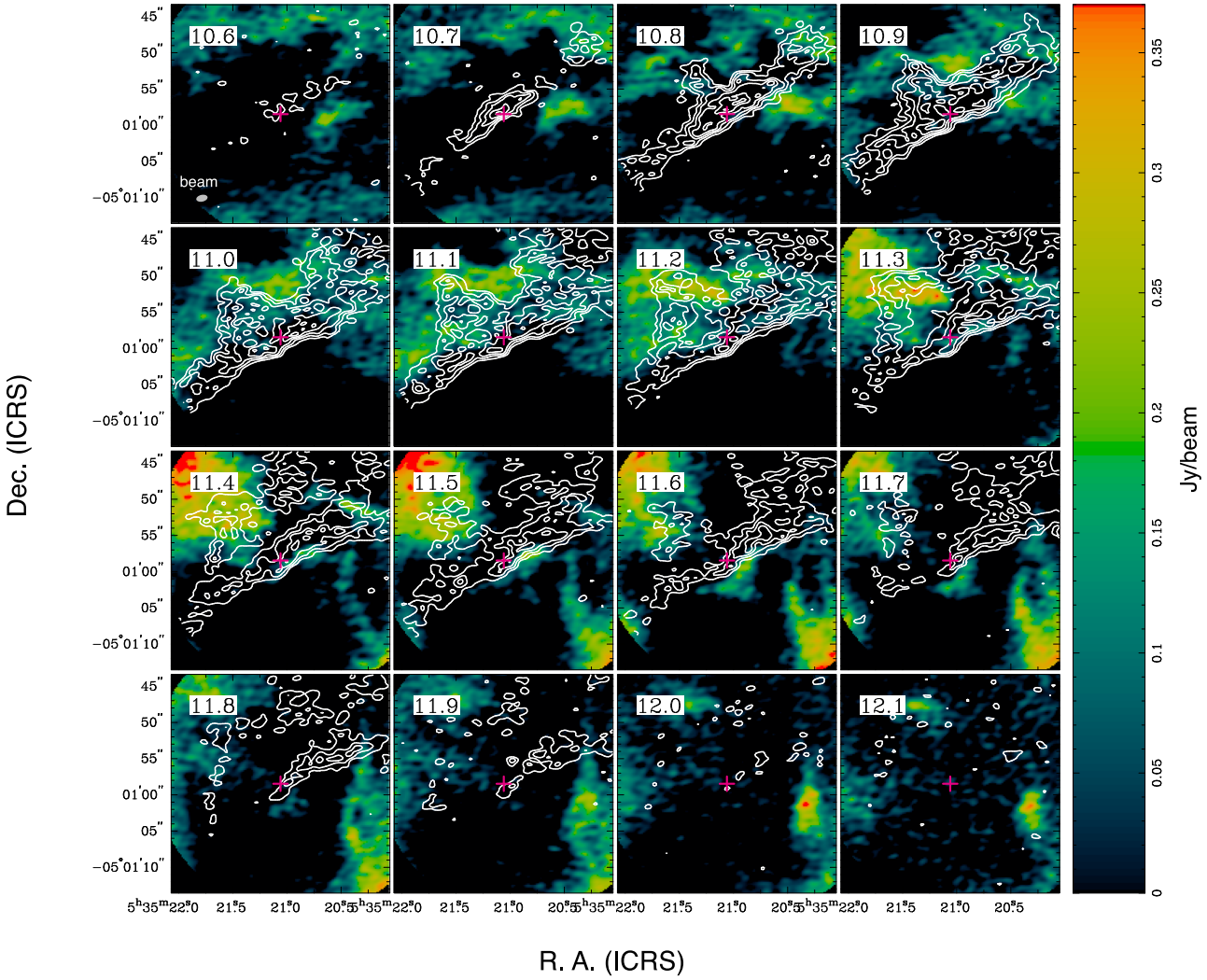

Figure A4. Channel maps of the $C^{18}O$ 2–1 (color) and N_2D^+ 3–2 (white contours) emission lines. The velocity resolution in 0.1 km s^{-1}. The magenta cross denotes the position of the nucleus.

Appendix B
Total Power Spectra

Figure B1 shows the ^{12}CO 2-1 and ^{13}CO 2-1 spectra obtained with the TP array.

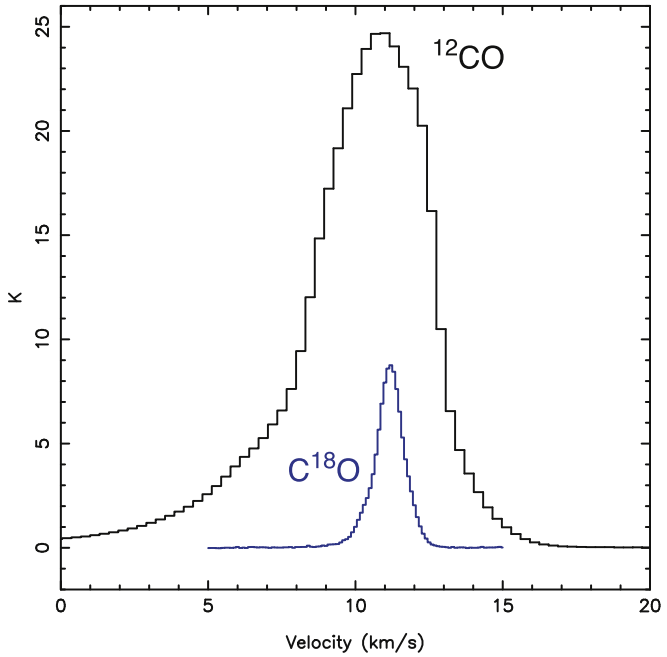

Figure B1. ^{12}CO and C^{18}O spectra toward the position of the nucleus obtained with the TP array. The beam size of the TP array is 28.″23 in ^{12}CO and is 29.″58 in C^{18}O.

ORCID iDs

Naomi Hirano https://orcid.org/0000-0001-9304-7884
Dipen Sahu https://orcid.org/0000-0002-4393-3463
Sheng-Yaun Liu https://orcid.org/0000-0003-4603-7119
Tie Liu https://orcid.org/0000-0002-5286-2564
Ken'ichi Tatematsu https://orcid.org/0000-0002-8149-8546
Somnath Dutta https://orcid.org/0000-0002-2338-4583
Shanghuo Li https://orcid.org/0000-0003-1275-5251
Chin-Fei Lee https://orcid.org/0000-0002-3024-5864
Pak Shing Li https://orcid.org/0000-0001-8077-7095
Shih-Ying Hsu https://orcid.org/0000-0002-1369-1563
Sheng-Jun Lin https://orcid.org/0000-0002-6868-4483
Doug Johnstone https://orcid.org/0000-0002-6773-459X
Leonardo Bronfman https://orcid.org/0000-0002-9574-8454
Huei-Ru Vivien Chen https://orcid.org/0000-0002-9774-1846
David J. Eden https://orcid.org/0000-0002-5881-3229
Yi-Jehng Kuan https://orcid.org/0000-0002-4336-0730
Woojin Kwon https://orcid.org/0000-0003-4022-4132
Chang Won Lee https://orcid.org/0000-0002-3179-6334
Hong-Li Liu https://orcid.org/0000-0003-3343-9645
Mark G. Rawlings https://orcid.org/0000-0002-6529-202X
Isabelle Ristorcelli https://orcid.org/0000-0002-1469-6323
Alessio Traficante https://orcid.org/0000-0003-1665-6402

References

Aikawa, Y., Wakelam, V., Garrod, R. T., & Herbst, E. 2008, ApJ, 674, 984
Aso, Y., Kwon, W., Hirano, N., et al. 2021, ApJ, 920, 71
Aso, Y., Tatematsu, K., Sekimoto, Y., et al. 2000, ApJS, 131, 465
Astropy Collaboration, Robitaille, T. P., Tollerud, E. J., et al. 2013, A&A, 558, A33
Bastien, P. 1983, A&A, 119, 109
Bertoldi, F., & McKee, C. F. 1992, ApJ, 395, 140
Bourke, T. L., Myers, P. C., Caselli, P., et al. 2012, ApJ, 745, 117
Burkert, A., & Hartmann, L. 2004, ApJ, 616, 288
Caselli, P., Pineda, J. E., Zhao, B., et al. 2019, ApJ, 874, 89
Caselli, P., Pineda, J. E., Sipilä, O., et al. 2022, ApJ, 929, 13
Caselli, P., Walmsley, C. M., Zucconi, A., et al. 2002, ApJ, 565, 344
Chacón-Tanarro, A., Caselli, P., Bizzocchi, L., et al. 2019, A&A, 622, A141
Chini, R., Reipurth, B., Ward-Thompson, D., et al. 1997, ApJL, 474, L135
Clarke, S. D., & Whitworth, A. P. 2015, MNRAS, 449, 1819
Commerçon, B., Launhardt, R., Dullemond, C., & Henning, T. 2012, A&A, 545, A98
Crapsi, A., Caselli, P., Walmsley, C. M., et al. 2005, ApJ, 619, 379
Crapsi, A., Caselli, P., Walmsley, M. C., & Tafalla, M. 2007, A&A, 470, 221
Crutcher, R. M. 2012, ARA&A, 50, 29
Daniel, F., Cernicharo, J., & Dubernet, M. L. 2006, ApJ, 648, 461
di Francesco, J., Evans, N. J. I., Caselli, P., et al. 2007, in Protostars and Planets V, ed. B. Reipurth, D. Jewitt, & K. Keil (Tucson, AZ: Univ. Arizona Press), 17
Dunham, M. M., Crapsi, A., Evans, N. J. I., et al. 2008, ApJS, 179, 249
Dutta, S., Lee, C.-F., Liu, T., et al. 2020, ApJS, 251, 20
Eden, D. J., Liu, T., Kim, K.-T., et al. 2019, MNRAS, 485, 2895
Fayolle, E. C., Balfe, J., Loomis, R., et al. 2016, ApJL, 816, L28
Frerking, M. A., Langer, W. D., & Wilson, R. W. 1982, ApJ, 262, 590
Friesen, R. K., Pon, A., Bourke, T. L., et al. 2018, ApJ, 869, 158
Furlan, E., Fischer, W. J., Ali, B., et al. 2016, ApJS, 224, 5
Garrod, R., Park, I. H., Caselli, P., & Herbst, E. 2006, FaDi, 133, 51
Garrod, R. T., & Herbst, E. 2006, A&A, 457, 927
Gerin, M., Pety, J., Fuente, A., et al. 2015, A&A, 577, L2
Girart, J. M., Rao, R., & Marrone, D. P. 2006, Sci, 313, 812
Hanawa, T., Yamamoto, S., & Hirahara, Y. 1994, ApJ, 420, 318
Hennebelle, P., & Inutsuka, S.-i 2019, FrASS, 6, 5
Herbst, E., & Cuppen, H. M. 2006, PNAS, 103, 12257
Houde, M., Dowell, C. D., Hildebrand, R. H., et al. 2004, ApJ, 604, 717
Huang, Y.-H., & Hirano, N. 2013, ApJ, 766, 131
Hull, C. L. H., Girart, J. M., Tychoniec, Ł., et al. 2017, ApJ, 847, 92
Kauffmann, J., Pillai, T., & Goldsmith, P. F. 2013, ApJ, 779, 185
Keto, E., & Caselli, P. 2010, MNRAS, 402, 1625
Kim, G., Tatematsu, K., Liu, T., et al. 2020, ApJS, 249, 33
Kong, S., Arce, H. G., Feddersen, J. R., et al. 2018, ApJS, 236, 25
Kounkel, M., Covey, K., Suárez, G., et al. 2018, AJ, 156, 84
Kounkel, M., Hartmann, L., Loinard, L., et al. 2017, ApJ, 834, 142
Li, D., Kauffmann, J., Zhang, Q., & Chen, W. 2013, ApJL, 768, L5
Li, P. S., Lopez-Rodriguez, E., Ajeddig, H., et al. 2022a, MNRAS, 510, 6085
Li, P. S., Lopez-Rodriguez, E., Soam, A., & Klein, R. I. 2022b, MNRAS, 514, 3024
Lis, D. C., Serabyn, E., Keene, J., et al. 1998, ApJ, 509, 299
Liu, T., Kim, K.-T., Juvela, M., et al. 2018, ApJS, 234, 28
Luo, Q.-y., Liu, T., Tatematsu, K., et al. 2022, ApJ, 931, 158
Mathis, J. S., Rumpl, W., & Nordsieck, K. H. 1977, ApJ, 217, 425
Matsushita, Y., Takahashi, S., Machida, M. N., & Tomisaka, K. 2019, ApJ, 871, 221
Matthews, B. C., Wilson, C. D., & Fiege, J. D. 2001, ApJ, 562, 400
McMullin, J. P., Waters, B., Schiebel, D., Young, W., & Golap, K. 2007, in ASP Conf. Ser. 376, Astronomical Data Analysis Software and Systems XVI, ed. R. A. Shaw, F. Hill, & D. J. Bell (San Francisco, CA: ASP), 127
Megeath, S. T., Gutermuth, R., Muzerolle, J., et al. 2012, AJ, 144, 192
Millar, T. J., Bennett, A., & Herbst, E. 1989, ApJ, 340, 906
Morii, K., Takahashi, S., & Machida, M. N. 2021, ApJ, 910, 148
Müller, H. S. P., Schlöder, F., Stutzki, J., & Winnewisser, G. 2005, JMoSt, 742, 215
Müller, H. S. P., Thorwirth, S., Roth, D. A., & Winnewisser, G. 2001, A&A, 370, L49
Nutter, D., & Ward-Thompson, D. 2007, MNRAS, 374, 1413
Öberg, K. I., van Broekhuizen, F., Fraser, H. J., et al. 2005, ApJL, 621, L33
Omukai, K. 2007, PASJ, 59, 589
Ossenkopf, V., & Henning, T. 1994, A&A, 291, 943
Ostriker, J. 1964, ApJ, 140, 1056
Pabst, C. H. M., Goicoechea, J. R., Teyssier, D., et al. 2020, A&A, 639, A2
Pezzuto, S., Elia, D., Schisano, E., et al. 2012, A&A, 547, A54
Planck Collaboration, Ade, P. A. R., Aghanim, N., et al. 2016, A&A, 594, A28
Pon, A., Johnstone, D., & Heitsch, F. 2011, ApJ, 740, 88
Pon, A., Toalá, J. A., Johnstone, D., et al. 2012, ApJ, 756, 145

Redaelli, E., Bizzocchi, L., Caselli, P., et al. 2019, A&A, 629, A15
Sahu, D., Liu, S.-Y., Liu, T., et al. 2021, ApJL, 907, L15
Saigo, K., Tomisaka, K., & Matsumoto, T. 2008, ApJ, 674, 997
Sault, R. J., Teuben, P. J., & Wright, M. C. H. 1995, in ASP Conf. Ser. 77, Astronomical Data Analysis Software and Systems IV, ed. R. A. Shaw, H. E. Payne, & J. J. E. Hayes (San Francisco, CA: ASP), 433
Schuller, F., André, P., Shimajiri, Y., et al. 2021, A&A, 651, A36
Shu, F. H. 1977, ApJ, 214, 488
Stodólkiewicz, J. S. 1963, AcA, 13, 30
Takahashi, S., Ho, P. T. P., Teixeira, P. S., Zapata, L. A., & Su, Y.-N. 2013, ApJ, 763, 57
Takahashi, S., Saito, M., Ohashi, N., et al. 2008, ApJ, 688, 344
Tatematsu, K., Kim, G., Liu, T., et al. 2021, ApJS, 256, 25
Tatematsu, K., Liu, T., Ohashi, S., et al. 2017, ApJS, 228, 12
Tatematsu, K., Yeh, Y.-T., Hirano, N., et al. 2022, ApJ, 931, 33
Tobin, J. J., Sheehan, P. D., Megeath, S. T., et al. 2020, ApJ, 890, 130
Tomisaka, K., Ikeuchi, S., & Nakamura, T. 1988, ApJ, 335, 239
Tritsis, A., Panopoulou, G. V., Mouschovias, T. C., Tassis, K., & Pavlidou, V. 2015, MNRAS, 451, 4384
Turner, B. E. 2001, ApJS, 136, 579
Vaytet, N., Audit, E., Chabrier, G., Commerçon, B., & Masson, J. 2012, A&A, 543, A60
Wannier, P. G. 1980, ARA&A, 18, 399
Ward-Thompson, D., André, P., Crutcher, R., et al. 2007, in Protostars and Planets V, ed. B. Reipurth, D. Jewitt, & K. Keil (Tucson, AZ: Univ. Arizona Press), 33
Williams, J. P., Plambeck, R. L., & Heyer, M. H. 2003, ApJ, 591, 1025
Wilson, T. L., & Rood, R. 1994, ARA&A, 32, 191
Wright, E. L., Eisenhardt, P. R. M., Mainzer, A. K., et al. 2010, AJ, 140, 1868
Yamamoto, S. 2017, Chemical Evolution from Interstellar Clouds to Star and Planet Formation (Tokyo: Springer)
Yi, H.-W., Lee, J.-E., Liu, T., et al. 2018, ApJS, 236, 51